catalysts

MDPI

Review

Platinum Alloys for Methanol Oxidation Electrocatalysis: Reaction Mechanism and Rational Design of Catalysts with Exceptional Activity and Stability

Renqin Yu [1,†], Yifan Zhang [2,†], Sixu Deng [3], Rongying Zhu [1], Shiming Zhang [1], Jiujun Zhang [1], Yufeng Zhao [1,*] and Zhonghong Xia [1,*]

[1] Institute for Sustainable Energy, College of Sciences, Shanghai University, No. 99 Shangda Road, Baoshan District, Shanghai 200444, China; yurenqin@shu.edu.cn (R.Y.); z1037479934@163.com (R.Z.); smzhang@shu.edu.cn (S.Z.); jiujun.zhang@i.shu.edu.cn (J.Z.)
[2] School of Environmental & Chemical Engineering, Shanghai University, No. 99 Shangda Road, Baoshan District, Shanghai 200444, China; zyf010626@shu.edu.cn
[3] Department of Chemical and Materials Engineering, Concordia University, Montreal, QC H3G 1M8, Canada; sixu.deng@concordia.ca
* Correspondence: yufengzhao@shu.edu.cn (Y.Z.); 10011493@shu.edu.cn (Z.X.)
† These authors contributed equally to this work.

Abstract: Direct methanol fuel cells have emerged as highly promising energy conversion devices in the past few decades. However, some challenges, such as carbon monoxide (CO) poisoning and unsatisfactory long-term stability, remain for platinum (Pt) as a methanol oxidation reaction (MOR) catalyst. This review covers recent advances in Pt alloy MOR catalysts and provides some insights. This review presents MOR catalytic mechanisms based on CO or non-CO pathways. Typical dimension-based designs of MOR catalysts, such as anisotropic nanowires, metallene, nanoframes, and corresponding rationales for performance enhancements, are introduced. More importantly, some key tuning strategies are elaborated, including intermetallic compound synthesis, interface engineering, and surface facet engineering. High-entropy alloys as an intriguing class of MOR catalysts with favorable prospects are also discussed. Finally, future directions and opportunities are outlined.

Keywords: methanol oxidation reaction; Pt alloys; intermetallic; interface engineering; surface facet engineering

Citation: Yu, R.; Zhang, Y.; Deng, S.; Zhu, R.; Zhang, S.; Zhang, J.; Zhao, Y.; Xia, Z. Platinum Alloys for Methanol Oxidation Electrocatalysis: Reaction Mechanism and Rational Design of Catalysts with Exceptional Activity and Stability. *Catalysts* **2024**, *14*, 60. https://doi.org/10.3390/catal14010060

Academic Editor: Barbara Mecheri

Received: 23 November 2023
Revised: 30 December 2023
Accepted: 9 January 2024
Published: 12 January 2024

1. Introduction

The overuse of fossil fuels has led to numerous problems, such as a worsening crisis and severe environmental pollution. Direct methanol fuel cells (DMFCs), an important type of proton exchange membrane fuel cells, have been extensively studied since they possess plenty of merits, including low cost, high energy conversion efficiency, convenient storage/transportation, and low greenhouse emissions [1–5]. The anode's methanol oxidation reaction (MOR) depends on reaction kinetics, and Pt is most commonly used as an electrocatalyst. However, Pt inevitably faces poisoning due to the strong adsorption of the intermediate carbon monoxide (CO) reaction, leading to weakened activity and stability. The development of an anodic catalyst that can resist CO poisoning is of primary importance. There are two basic solutions: one is to diminish the CO adsorption strength by modulation of the electronic structure of Pt-based catalysts, and the second is to facilitate CO electro-oxidation by an oxygenated species, such as OH at a lower potential, both of which can be attained by doping with diverse elements [2,4,6–8].

Numerous Pt-based alloys have been proposed as highly efficient MOR catalysts [6,9–12]. Pt-based solid solution alloys with foreign elements doped into a Pt lattice provide sufficient compositional and electronic tuning possibilities. Intermetallic compounds with exceptionally

negative enthalpies of formation and strong atomic (orbital) interaction endow them with remarkable activity and anti-corrosion stability [13–15]. Also, the intrinsic catalytic activity of core–shell structures can be tailored by altering the shell thickness [16–18]. The chemisorption energy of adsorbates, such as reactants and intermediates, can be engineered by varying the Pt d-band center associated with the electronic effects [19].

This review first overviews the MOR reaction mechanism, i.e., CO and non-CO pathways. The electronic modulation, which plays a vital role in enhancing catalytic activity, will be presented as fundamentals for MOR catalyst design. Then, MOR catalysts with dimensions spanning from 1-dimension to 3-dimension are introduced. After that, typical enhancing strategies are thoroughly discussed, including the application of intermetallic compounds to MOR catalysis, interface engineering to tune the electronic structure and surface facet engineering. Last but not least, recent progress with respect to high-entropy alloys as highly efficient MOR catalysts is highlighted.

2. MOR Catalytic Pathways: CO Pathways and Non-CO Pathways

The catalytic pathways involving various intermediate species are still under debate, which makes it necessary to unravel the reaction mechanism and add insight into the enhanced catalytic performances. The incomplete oxidation products of methanol are formic acid and/or CO, and the complete oxidation outcome is CO_2 (through a six-electron transfer process). This section introduces the MOR catalytic mechanism with the aim of more precisely tuning the catalyst structure and elevating performance.

Methanol oxidation mainly generates CO_2, although plenty of CO* and COOH* species are also formed during reactions. Generally, the adsorption of methanol, followed by its dehydrogenation to form CO*, and desorptive oxidation of CO* are commonly considered critical steps for MOR catalysis. Platinum-based multimetallic catalysts offer an effective strategy to address CO poisoning at the present stage, wherein the paths for methanol dissociation and Pt electrode absorption are as follows:

$$Pt + CH_3OH \rightarrow Pt\text{-}(CH_3OH)_{ads} \rightarrow Pt\text{-}(CO)_{ads} + 4H^+ + 4e^- \quad (1)$$

$$M + H_2O \rightarrow M\text{-}OH_{ads} + H^+ + e^- \quad (2)$$

$$Pt\text{-}(CO)_{ads} + M\text{-}OH_{ads} \rightarrow Pt + M + CO_2 + H^+ + e^- \quad (3)$$

wherein M denotes a second metal. In step (1), methanol adsorbed on the Pt sites undergoes C-H and O-H bond splitting to produce CO_{ads} intermediate. Step (2) involves water dissociation to generate OH_{ads} species, and step (3) is the oxidation of CO_{ads} by OH_{ads} to produce CO_2. The CO_{ads} formation, a spontaneously favored process with fast kinetics, results in a poisoning effect and impedes further methanol oxidation.

The incorporation of second elements (Rh, Ru, Sn, etc.) has been widely utilized to generate oxygenated species at low potentials to mitigate toxic CO_{ads} species. Sheng et al. investigated the MOR mechanism by unraveling the role of Rh doped on Pt(111) at the atomic scale [8]. The $CH_3OH^* \rightarrow CH_2OH^* \rightarrow CHOH^* \rightarrow CHO^* \rightarrow CO^*$ transformation proceeds on both Rh*/Pt(111) and Rh/Pt*(111) catalysts. The rate-determining step of methanol dehydrogenation on both catalysts is $CH_3OH^* \rightarrow CH_2OH^*$ with C-H bond splitting. The existence of Rh sites lowers kinetic barriers of methanol dehydrogenation considerably relative to Pt sites. At lower potential, Rh sites contribute to the methanol dehydrogenation due to a small amount of adsorbed OH*. In comparison, at a higher potential of around 0.6 V, Rh sites serve to activate water for the generation of OH*, considering Rh sites are substantially covered by OH*. Wang et al. synthesized Rh-reinforced quatermetallic ultrathin PtCoNiRh nanowires [20]. Rh-decorated Pt-skin $Pt_3Co_{0.5}Ni_{0.5}(111)$ and Pt-skin $Pt_3Co_{0.5}Ni_{0.5}(111)$ were constructed to reveal the effect of Rh doping on the reaction pathway. The MOR pathway of Pt-skin $Pt_3Co_{0.5}Ni_{0.5}(111)$ is as follows: $CH_3OH \rightarrow CH_3OH^* \rightarrow CH_3O^* \rightarrow CH_2O^* \rightarrow CHO^* \rightarrow CO^* \rightarrow COOH^* \rightarrow CO_2$ (Figure 1). Nevertheless, the thermodynamically favorable reaction path on Rh-decorated Pt-skin $Pt_3Co_{0.5}Ni_{0.5}(111)$ is as follows: $CH_3OH \rightarrow CH_3OH^* \rightarrow CH_2OH^* \rightarrow CHOH^* \rightarrow COH^*$

→ CO* → COOH* → CO_2. On the surface of Rh-decorated Pt-skin $Pt_3Co_{0.5}Ni_{0.5}$(111), CH_3OH* is inclined to form CH_2OH* by dissociating the C-H bond rather than the O-H bond in the initial dehydrogenation. Moreover, the Rh-decorated catalyst is more prone to break the C-H bond of CHOH* to generate stable COH* rather than CHO* owing to the more negative free energy change of CHOH* → COH* transformation. Of note is that the formation of COOH* (CO* + OH* → COOH*) is a rate-limiting step for both catalysts. The Rh-decorated catalyst with the lower COOH* formation energy (0.76 eV) relative to the non-Rh counterpart (0.91 eV) corresponds to easier surface OH* generation and CO* oxidation. Then, the generated COOH* adsorbs on the Rh site to release H^+ to form CO_2.

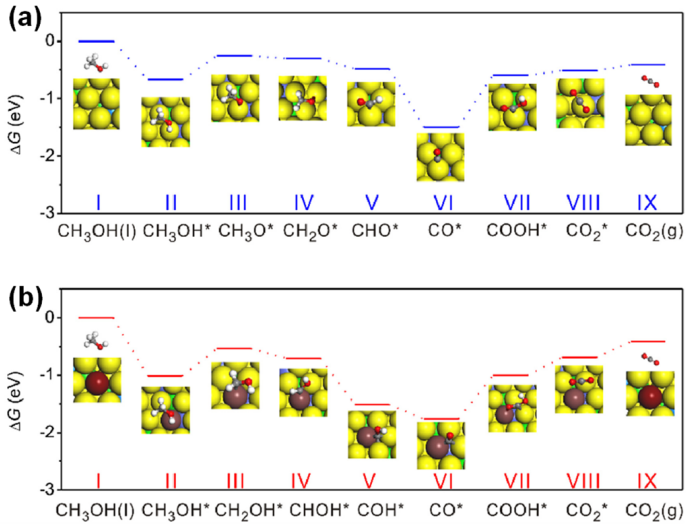

Figure 1. Free energy diagrams and optimized structures of MOR intermediates on (**a**) Rh-free Pt-skin $Pt_3Co_{0.5}Ni_{0.5}$(111) surfaces and (**b**) Rh-decorated Pt-skin $Pt_3Co_{0.5}Ni_{0.5}$(111) surfaces. Reprinted with permission from Ref. [20]. Copyright 2020, Elsevier Ltd.

On the other hand, some provide experimental and theoretical demonstrations of the non-CO-generation pathway during MOR catalysis. The evolution of key intermediates can usually be revealed by in situ Fourier-transform infrared (FTIR) spectroscopy analysis [21–23]. Qi et al. prepared 3.2 nm-PtZn intermetallic nanoparticles grown on multiwalled carbon nanotube (MWNT) via chemical etching of PtZn/MWNT confined by a mesoporous SiO_2 shell [24]. The theoretical calculations of the small-sized PtZn intermetallic nanoparticles demonstrate the thermodynamically favorable non-CO pathway of CH_3OH* → CH_2OH* → CH_2O*→ H_2COOH* → HCOOH* → HCOO* → CO_2, while the large thermodynamic sink of CO formation on Pt makes it quite difficult to attain CO* → COOH* conversion. Wang et al. synthesized $Pt_{92}Bi_8$ surface alloy with a Pt-rich core [25]. The in situ attenuated total reflection surface-enhanced infrared absorption (ATR-SEIRA) spectra reveal that contrary to the co-existence of CO and formate ($HCOO^-$) pathways for MOR on Pt nanoparticles, the incorporation of Bi inhibits CO formation thermodynamically and kinetically. The CO_2 on $Pt_{92}Bi_8$ stems from a formate, especially at high potentials (>0.5 V), due to the presence of abundant OH_{ad}. Similarly, our research on $Pt_{64}Fe_{20}Ir_{16}$ and $Pt_{65}Fe_{22}Ir_{13}$ jagged nanowires shows that the formate peak intensity of in situ FTIR spectra increases concomitantly with the attenuated CO peak as potential increases (Figure 2a–c) [26]. In contrast, the absence of an HCOOads peak and an undiminished CO_L peak prove the strong inclination toward the CO pathway on Pt/C. Zhao et al. synthesized a Cu-doped PtBi alloy catalyst with Cu atoms highly interspersed within the nanoparticles [22]. The in situ FTIR studies reveal the non-CO pathway by $Pt_{69.2}Bi_{29.6}Cu_{1.2}$ and Pt_3Bi alloy and the CO pathway for Pt black (Figure 2d–f). The attenuation of $HCOO^-$ intensity for $Pt_{69.2}Bi_{29.6}Cu_{1.2}$ after 0.1 V indicates faster kinetics of $HCOO^-$ → CO_2 relative to Pt_3Bi and Pt black. Moreover, the diminished intensity of the CO_2 peak and the increased

intensity of the CO_3^{2-}/HCO_3^- peak for $Pt_{69.2}Bi_{29.6}Cu_{1.2}$ demonstrate weakened adsorption of CO_2 and faster $CO_2 \rightarrow CO_3^{2-}/HCO_3^-$ conversion, which are probable reasons why $Pt_{69.2}Bi_{29.6}Cu_{1.2}$ outperforms the Pt_3Bi alloy and Pt black.

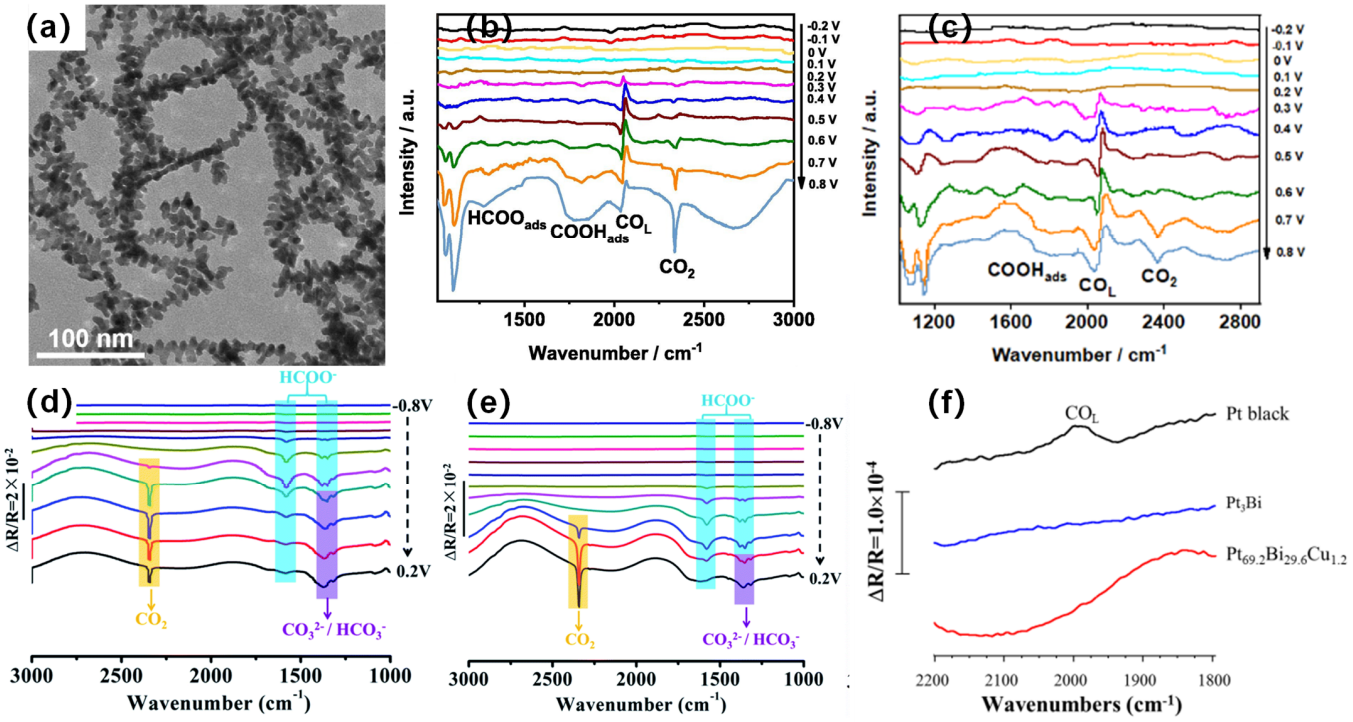

Figure 2. (**a**) Transmission electron microscopy (TEM) image of $Pt_{64}Fe_{20}Ir_{16}$ jagged nanowires. Potential-resolved in situ FTIR spectra of CO_2, $CO_{L,}$ and $HCOO_{ads}$ as a function of the potential on (**b**) $Pt_{64}Fe_{20}Ir_{16}$ jagged nanowires and (**c**) Pt/C. Reprinted with permission from Ref. [26]. Copyright 2023, Elsevier Ltd. In situ FTIR spectra of (**d**) $Pt_{69.2}Bi_{29.6}Cu_{1.2}$ nanoalloy and (**e**) intermetallic Pt_3Bi nanocrystals ranging from −0.8 V to 0.2 V at the potential step of 0.1 V. (**f**) Enlarged picture between 2200 cm^{-1} and 1800 cm^{-1}. Reprinted with permission from Ref. [22]. Copyright 2020, Royal Society of Chemistry.

Differential electrochemical mass spectrometry (DEMS) is an effective tool in terms of the detection of MOR intermediate species. Zeng et al. demonstrated MOR catalytic mechanisms for PtFeCu ternary intermetallic catalysts via DEMS [27]. Initial C-H bond cleavage gives rise to CH_2OH_{ad}, which is further dehydrogenated to HCO_{ad}. At a low potential of <0.7 V, the adsorption of H_2O by HCO_{ad} gives rise to $CH(OH)_2$ and finally to HCOOH since CO_{ad} species derived from HCO_{ad} is highly stable. In contrast, at a high potential for CO_{ads} oxidative desorption, HCOOH can be converted to CO_2 directly or indirectly via a CO_{ad} intermediate. By DEMS examination, the $HCOOCH_3$ formation efficiency, as a measure of HCOOH formation, is the highest for $PtFe_{0.5}Cu_{0.5}$ as Cu is continuously incorporated into PtFe. The lattice contraction due to Cu incorporation leads to stabilized adsorption of intermediates like $CH(OH)_2$, which favors the $CH(OH)_2 \rightarrow HCOOH \rightarrow CO_2$ direct pathway. Combining recent representative reports of the dual-pathway mechanisms via in situ FTIR and DEMS characterization, a whole picture is provided in Scheme 1.

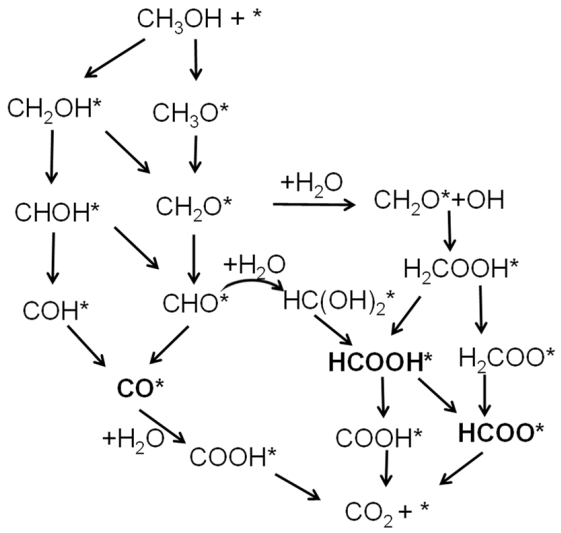

Scheme 1. A schematic illustration of CO and non-CO MOR pathways. * denotes adsorption sites.

3. Electronic Effects on Catalytic Performance

The electronic effect is typically manifested by the variation of the Pt d-band center owing to the electron transfer between constituent elements with different electronegativity. Several reports show that introducing a foreign metal suppresses the Pt d-band center with a relieved overbinding effect toward reaction intermediates such as CO [28–30]. The downshift of the Pt d-band center occurs concomitantly with increased *d* states being pulled below the Fermi level [17,31,32]. The *d*-band center variation is commonly demonstrated by the negative shift of binding energy in Pt XPS spectra. Moreover, the high electron density of foreign metals near the Fermi level facilitates the charge transfer from catalyst to adsorbate molecules. Meanwhile, foreign metals with broad orbital ranges across the Fermi level usually play a pivotal role in protecting Pt sites' robust and stable electronic structure while accelerating site-to-site charge transfer on the catalyst surface [33–35].

Using a PtBiZn nanoplate as an archetype of electronic effect, Tian et al. demonstrated that the CO* → COOH* free energy change reduces from 0.37 eV of PtBi to 0.28 eV of PtBiZn-1, suggestive of weakened CO adsorption and mitigated CO poisoning (Figure 3) [2]. This is closely correlated to the downshift of the *d*-band center from −2.71 eV of PtBi to −2.95 eV of PtBiZn-1. The CO adsorption energy drops from −1.96 eV of PtBi surface to −1.73 eV of PtBiZn-1 surface. Zhang et al. demonstrated that for PtNiRh ultrathin nanowires, the *d*–*d* charge transfer of delocalized Ni 3*d* and electron-rich Rh 4*d* orbitals synergistically pinned Pt 5*d* center at a position close to the Fermi level with a balance between the noticeably suppressed CO adsorption due to limited orbital overlap and reduced reaction barrier of methanol oxidation [4]. Luo et al. utilized electron-spin engineering for MOR catalysis using PdFePt nanomeshes [36]. The moderate incorporation of Fe with a high electron occupancy in the e_g orbital promotes its overlap with the O p_z orbital, which facilitates the adsorption of oxygenated intermediates (OH_{ads}). Flexible electronic modulations with multiple orbital hybridization help to attain the optimal binding strength of reactants and intermediate species. The coordination environment also influences catalytic activity via variation in the *d*-band center. The empirical rule is that the *d*-band center shifts downward with larger *d*-band width (stronger orbital hybridization) as a result of the increased coordination number [29].

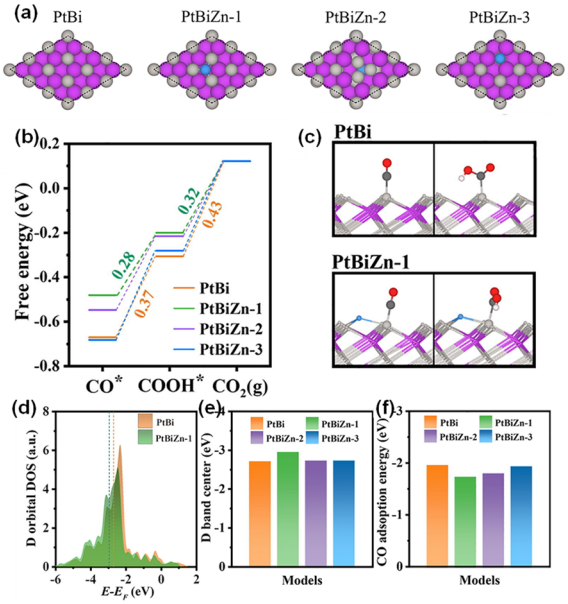

Figure 3. Electronic mechanisms of PtBi and PtBiZn. (**a**) PtBi and PtBiZn structures. Zn deposited on the surface, Zn replacing one sub-surface Bi atom, and Zn replacing one surface Pt atom are specified as PtBiZn-1, PtBiZn-2, and PtBiZn-3, respectively. (**b**) Free energy changes of key steps. (**c**) CO* → COOH* adsorption configurations on the PtBi and PtBiZn-1 surface. (**d**) D-orbital density of states. (**e**) D-band centers. (**f**) CO adsorption energies. Reprinted with permission from Ref. [2]. Copyright 2022, Elsevier Ltd.

4. Dimensional Engineering of Pt-Based Alloys for MOR

Ultrathin nanowires with a diameter of less than 2 nm are usually considered promising MOR catalysts since surface active sites can be better exposed. Li et al. synthesized 22% YO_x/MoO_x-Pt ultrathin nanowires with superb MOR mass activity (2.10 A mg_{Pt}^{-1}) and specific activity (3.25 mA cm^{-2}) (Figure 4) [1]. The decoupling mechanism was proposed between CO_{ads} and $COOH_{ads}$, wherein $COOH_{ads}$ intermediate is adsorbed on the catalyst surface with C bound to Pt and O bound to oxophilic Y. The energy change for CO_{ads} oxidation to $COOH_{ads}$ (0.20 eV) is, therefore, considerably reduced compared to pure Pt (0.98 eV). The 22% YO_x/MoO_x–Pt ultrathin nanowires follow the reaction pathway $CH_3OH \rightarrow CH_2OH^* \rightarrow CH_2O^* \rightarrow CHO^* \rightarrow CO^* \rightarrow COOH^* \rightarrow CO_2$. Zhang et al. demonstrated the remarkable advantage of surface defects featured by void structures at the grain boundaries of Pd_4Sn wavy nanowires toward the MOR catalysis [37]. The high density of surface defects available in Pd_4Sn wavy nanowires provides more channels for the adsorption of small molecules. Thermodynamically, the surface void structure facilitates MOR catalysis in the HCOOH ($HCOO_{ads}$) pathway rather than the CO formation pathway. Moreover, the synergistic effect that occurs as noticeable structural distortion around Sn sites is balanced by local relaxations at Pd sites.

In recent years, noble metal-based metallenes have emerged as a highly efficient class of two-dimensional electrocatalysts owing to their considerably high atomic utilization, specific surface area, and exposure to active sites [38–48]. The optimized contact of the electrocatalysts with supports is also guaranteed through the construction of such two-dimensional materials. On the other hand, their crimped structure, which is suggestive of electronic modulation and the inner strain effect, may play a crucial role in enhancing the tolerance toward poisoning species (such as CO_{ads}) due to weakened adsorption strength. Wu et al. combined PdMo bimetallene with hydride by considering that Mo introduction improves hydrogen binding [49]. At 180 °C, high coverage of CO derived from $Mo(CO)_6$ hinders hydrogen penetration into the PdMo lattice, whereas PdMoH bimetallene can be formed with decreased CO concentration on PdMo surfaces at 220 °C. The PdMoH bimetallene possesses mass activity and specific activity of 3.56 A mg^{-1} and 6.06 mA cm^{-2},

far outperforming those of PdMo bimetallene. Tian et al. introduced various third metals (Co, Ni, Cu, Zn, Sn) into PtBi nanoplates for noticeably enhanced MOR catalytic activities [2]. It turned out that Zn-incorporated Pt_3Bi_3Zn nanoplates display the highest mass activity of 3.29 A mg_{Pt}^{-1}. The Zn incorporation leads to the downshift of the *d*-band center from −2.71 eV (PtBi) to −2.95 eV. The CO adsorption energy, therefore, becomes attenuated from −1.96 eV to −1.73 eV.

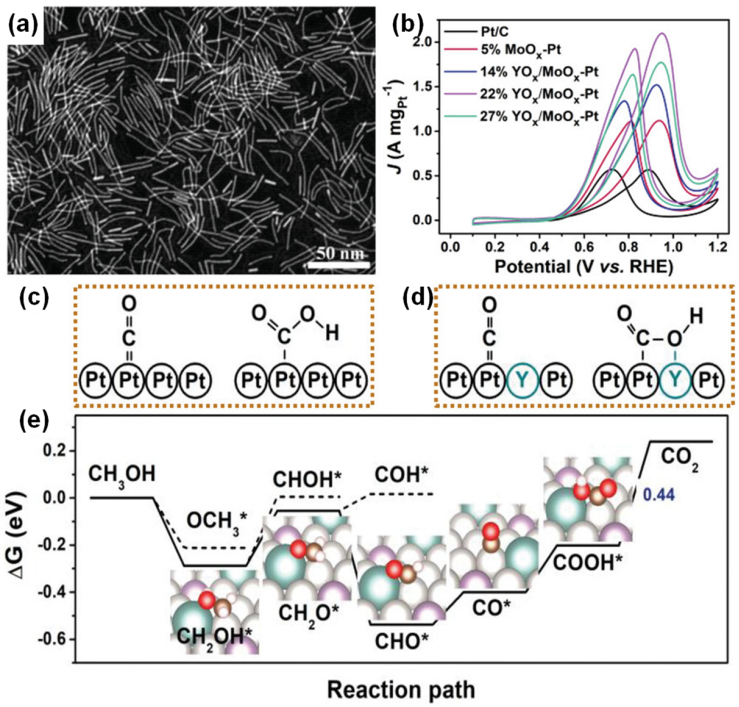

Figure 4. (**a**) High-angle annular dark-field scanning transmission electron microscopy (HAADF-STEM) image of 22% YO_x/MoO_x–Pt ultrathin nanowires. (**b**) Pt mass-normalized MOR cyclic voltammograms (CVs). Adsorption strategies for CO* and COOH* on (**c**) pure Pt and (**d**) $YO_x(MoO_x)$-decorated Pt surfaces. (**e**) Free energy diagram for MOR catalysis on YO_x/MoO_x–Pt surface. Reprinted with permission from Ref. [1]. Copyright 2021, Wiley-VCH GmbH.

Moreover, morphologically anisotropic superstructures have recently been reported to be beneficial for methanol oxidation catalysis [50–58]. The distorted Pt superstructures were prepared by electrochemical Te removal via 500 voltammetric cycles of $PtTe_x$ superstructures with tubular-like layered assembly structure in an acidic solution [50]. The flexible nanosheets with abundant nanopores, together with significant exposure of Pt catalytic sites due to massive Te leaching, contribute to an enhanced MOR activity of 2.89 A mg_{Pt}^{-1} with a 5.7-fold improvement relative to Pt/C. Their work also shows that as Te content increases from $PtTe_{1.0}$ to $PtTe_{1.5}$ to $PtTe_{2.0}$, the MOR activities of etched Pt superstructures follow the same increasing trend. The PtPdCu hollow sponges with hierarchically fractal pores were synthesized by Xiao et al. The mass activity and specific activity of 1.34 A mg_{Pt}^{-1} and 3.24 mA cm^{-2} were attained by PtPdCu hollow sponges as opposed to 0.34 A mg_{Pt}^{-1} and 0.44 mA cm^{-2} of Pt/C [56]. The hierarchically fractal pores of PtPdCu assist in the directed mass transfer from subpores to main pores and directed electron transfer from the thicker walls of the large-sized pores to the thinner walls of the small-sized pores, the latter of which promotes the favorable adsorption of methanol molecules. Moreover, the superior anti-CO poisoning capability, as manifested by the significantly lower CO oxidation onset potential (0.767 V of PtPdCu hollow sponges vs. 0.851 V of Pt/C), can be attributed to the dominant (111) facets.

In particular, nanoframes, a class of three-dimensional open and interconnected structures created through the spatial segregation of compositional elements, have garnered research

attention in recent years [59–64]. Composition segregation, also known as composition anisotropy, is the migration or rearrangement of different elements toward different regions. The overall Gibbs free energy must be minimized, with elements with a larger surface energy migrating towards the apex, edge, or corner to release the internal strain and elements with a lower surface energy prone to form the facet of the final nanocrystals [64]. Chen et al. synthesized PtCo rhombic dodecahedra with Pt located on the edges and Co uniformly located on the nanocrystals [62]. Nitric acid corrosion gives rise to the PtCo nanoframes. The powder X-ray diffraction pattern substantiates the formation of the PtCo nanoframe via the evolution from Pt-rich and Co-rich dual phases in $Pt_{23}Co_{77}$ to a Pt-rich single phase in $Pt_{82}Co_{18}$. The MOR catalysis by PtCo nanoframes exhibits 8.56 mA cm^{-2} with 5-fold enhancements relative to Pt/C in 1 M KOH + 1 M methanol. Similarly, Ding et al. synthesized composition-separated tetrahexahedral PtNi nanocrystals (THH PtNi NCs) and rhombic dodecahedral PtNi nanocrystals (RDH PtNi NCs) simply by adjusting oleylamine/oleic acid ratio, both of which are featured by homogeneous distribution of Ni across the whole facet and segregated location of Pt on the edges (Figure 5) [63]. The former product can be indexed to face-centered cubic (*fcc*) PtNi/$PtNi_3$ crystalline phases, while the latter is a combination of *fcc* $PtNi_2$/$PtNi_5$ phases. The acetic acid treatment of THH PtNi NCs and RDH PtNi NCs gives rise to tetrahexahedral PtNi nanoframes (THH PtNi NFs) and rhombic dodecahedral PtNi nanoframes (RDH PtNi NFs) with a pure alloy phase of *fcc* pattern. The THH PtNi NFs and RDH PtNi NFs exhibit exceptional specific activities of 2.19 mA cm^{-2} and 1.90 mA cm^{-2}, respectively. This is 3.91-fold and 3.39-fold higher than that of commercial Pt/C (0.56 mA cm^{-2}). Shang et al. reported the preparation of PtRuNi nanoframes surrounded by ultrathin Ru nanodendrites (PtRuNi FDs) [53]. The structure evolves into PtRuNi nanodendrites when increasing the amount of Ni precursor. The PtRuNi FDs exhibit a 2.9-fold improvement of MOR activity compared to Pt/C (1.49 A mg_{Pt}^{-1} vs. 0.52 A mg_{Pt}^{-1}).

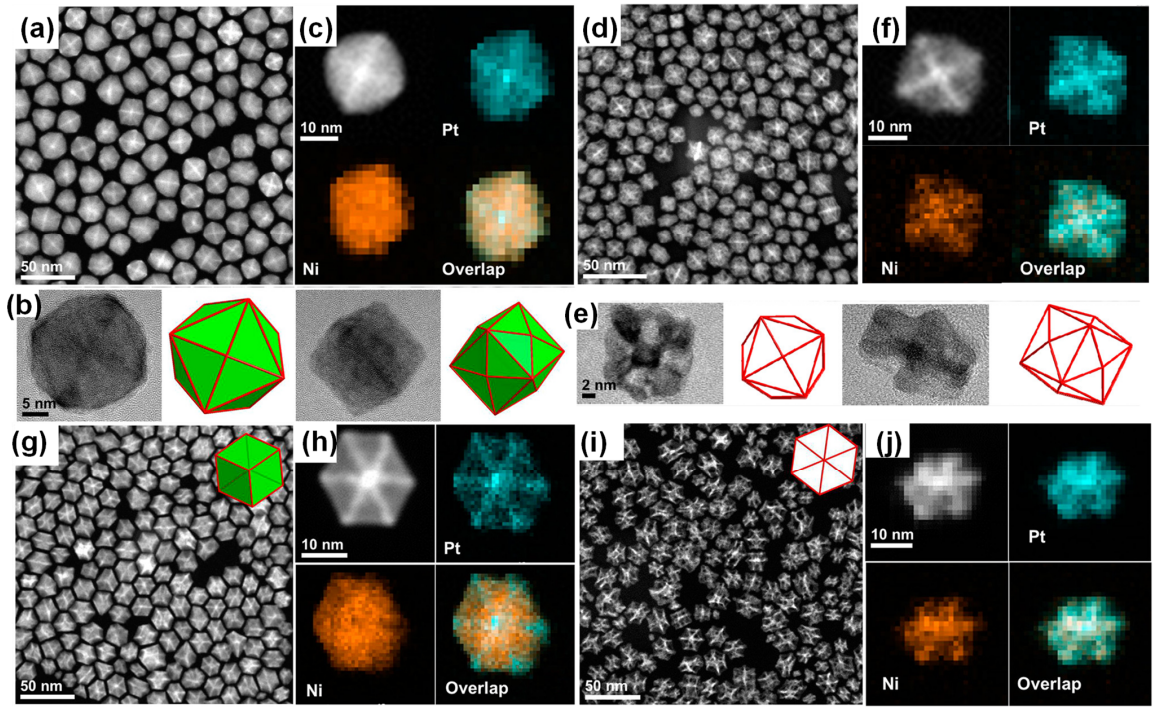

Figure 5. (**a**) HAADF-STEM image of THH PtNi nanocrystals. (**b**) TEM images and corresponding geometric models along two zone axes. (**c**) Elemental mappings for an individual nanocrystal. (**d**) HAADF-STEM image of THH PtNi nanoframes. (**e**) TEM images and geometric models along two zone axes. (**f**) Elemental mappings for an individual nanoframe. (**g**) HAADF-STEM image of RDH PtNi nanocrystals. (**h**) Elemental mappings for an individual RDH nanocrystal. (**i**) HAADF-STEM image of RDH PtNi nanoframes. (**j**) Elemental mappings for individual RDH nanoframes. Reprinted with permission from Ref. [63]. Copyright 2016, American Chemical Society.

5. Strategies to Enhance Activity and Stability

This section focuses on strategies to heighten catalyst activity and stability by modulating the internal ordering arrangement of atoms, interfacial modulation of electronic structure, and surface facet regulation in MOR catalysis. At the beginning of the section, it should be pointed out that core–shell structured catalysts are usually constructed to enhance electrocatalytic activity. Core–shell catalysts are mostly synthesized by electrochemical dealloying/leaching, adsorbate/thermal-induced segregation, galvanic displacement of underpotentially deposited Cu monolayer, and a one-step co-reduction approach [16–18,65–68]. The shell thickness of the core–shell structure can be engineered for optimal binding strength of adsorbates. The electronic effects generally lessen and vanish for the shell's three or more atomic layers. In comparison, lattice strain resulting from the difference in core and shell lattice parameters becomes attenuated or more than five atomic layers [69,70].

5.1. Intermetallic Compounds

Before delving into the section on intermetallic compounds as MOR catalysts, it is necessary to differentiate between random alloys and intermetallic compounds. In this context, "alloy" refers to random alloys and intermetallic compounds. The former, which can also be referred to as "solid solution", refers to the random or disordered mixing of "solute elements" (such as Fe, Co, Cu, etc.) into the lattice structure of "solvent elements" (such as Pt in our case). Constituent elements are, as the name suggests, in random stoichiometric ratios. For instance, the abovementioned quatermetallic ultrathin PtCoNiRh nanowires with Pt:Co:Ni:Rh atomic ratio of 64:11:12:13 exhibit a typical Pt *fcc* structure and a positive shift of diffraction peaks relative to Pt, the latter of which stems from the compressed lattice due to the incorporation of Co, Ni, and Rh with smaller lattice parameters [20].

Intermetallics with unique electronic structures have attracted extensive attention for their high catalytic performance [24,27,71–85]. Owing to their ordered atomic arrangement and evenly distributed active sites, they possess intrinsic stability compared to their solid solution alloy counterparts, making them highly active and reliable as versatile catalysts in energy conversion devices. Therefore, unveiling and modulating their electronic effects has become a notable topic for catalyst researchers. Qin et al. fabricated PtBi/Pt core–shell nanoplates composed of an intermetallic PtBi core with a hexagonal close-packed (hcp) phase, $P6_3/mmc$ space group, and *fcc* Pt shell [80]. The product achieves a mass activity of 1.1 A mg_{Pt}^{-1} and a specific activity of 3.18 mA cm^{-2}, 3.7-fold and 7.4-fold higher than Pt/C, respectively. Zhu et al. prepared a class of $PtFe_xCu_{1-x}$ intermetallic catalysts for efficient methanol oxidation [82]. The PtFe with disordered *fcc* structure annealed at 500 °C (PtFe-500). It evolved into $PtFe_{0.9}Cu_{0.1}$ with an ordered body-centered tetragonal (*bct*) structure after the incorporation of a tiny amount of Cu into the lattice. The PtFe annealed at 700 °C with an ordered *bct* phase (PtFe-700) retains a higher current density than its *fcc*-structured PtFe-500 counterpart after chronoamperometric measurement at 0.8 V for 3000 s. Furthermore, the $PtFe_{0.7}Cu_{0.3}$-700 catalyst with a robust *bct* ordered structure further inhibits Fe dissolution as compared to PtFe-700. The optimal Cu doping content in the PtFe0.7Cu0.3 catalyst improves considerably with only 11% Fe loss, in contrast to around 22% Fe loss for $PtFe_{0.9}Cu_{0.1}$ and PtFe.

The strain effect is usually manifested in Pt-based intermetallic catalysts with core-shell structures. Bu et al. synthesized a PtPb/Pt core/shell nanoplate catalyst with a PtPb intermetallic-phased nanoplate core that is 4.5 nm thick and a Pt shell that is 4~6 atomic layers thick [86]. Under biaxial strains of tensile strain along [001] direction and compressive strain along [110] direction, the low-coordinated bridge sites along [110] direction on the top and edge of the Pt surfaces serve as active sites due to weakened binding strength toward oxygenated species. This unique characteristic endows the catalyst with ORR and MOR-specific activities of 7.8 and 2.7 mA cm^{-2}, respectively. Li et al. prepared an L10-CoPtAu ternary intermetallic catalyst with an L10-PtCo core with Co stabilization and a two-atomic-layer AuPt shell as a result of Au enrichment on the surface [87]. The

surface compressive strain exerted on the AuPt shell, due to the smaller lattice parameter of PtCo core, mitigates the poisoning of carbonaceous species such as CO_{ads} due to the lowered *d*-band center of surface Pt. Unlike the A1-CoPtAu catalyst with Au embedded in the solid solution structure that undergoes acid etching of Co, the $L1_0$-CoPtAu intermetallic catalyst exhibits a mass activity of around 1.49 A/mg_{Pt}. Chen et al. examined the effect of annealing time on the MOR activity of $L1_2$-phased Pt_3Mn@Pt-skin. As the annealing time increases from 1 min to 24 h, the ordering degree increases, and the lattice parameter of the Pt_3Mn intermetallic core decreases (Figure 6) [73]. The Pt skin is, therefore, subject to increasing compressive strain induced by the Pt_3Mn core, wherein the nearest-neighboring Pt–Pt distance decreases continuously. The product obtained by 24 h-annealing is the most efficient catalyst in terms of MOR specific (2.71 mA cm^{-2}) and mass activity (1.98 A $mg_{Pt}{}^{-1}$). Further theoretical calculations demonstrate that compressive strain rather than ligand effect leads to improvement in the MOR activity of Pt_3Mn@Pt catalysts. Feng et al. synthesized an intermetallic Pt_3Ga catalyst with pure Pt of two to three atomic layers as a shell (AL-Pt/Pt_3Ga) [76]. The surface AL-Pt undergoes a tensile strain of 3.2% along the [100] direction and negligible strain along the [100] and [010] direction. The strong OH_{ads} adsorption AL-Pt owing to the upshift of the Pt *d*-band center indicates preferable water dissociation to remove poisonous CO_{ads} species. Every step of the conversion of $CH_3OH_{ads} \rightarrow CH_2OH_{ads} \rightarrow CHOH_{ads} \rightarrow COH_{ads} \rightarrow CO_{ads} \rightarrow CO_{ads} + OH_{ads}$ is energetically favorable on tensile strained Pt layers relative to pure Pt. The AL-Pt/Pt_3Ga exhibits a mass activity and specific activity of 1.094 A $mg_{Pt}{}^{-1}$ and 7.195 mA cm^{-2}, which are 1.9-fold and 8.5-fold higher than commercial Pt/C, respectively.

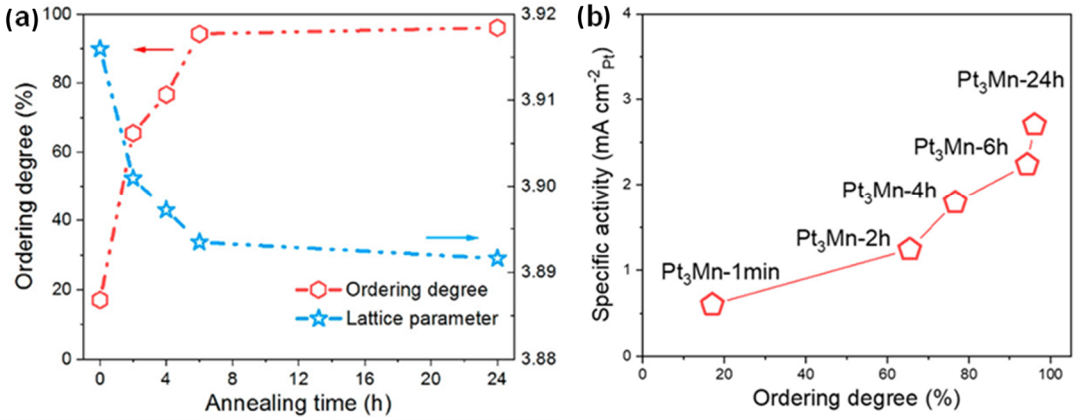

Figure 6. (**a**) Correlation between annealing time and ordering degree/lattice parameter of Pt_3Mn catalysts. (**b**) Correlation between specific activity at 0.8 V and the ordering degree of Pt_3Mn. Reprinted with permission from Ref. [73]. Copyright 2022, American Chemical Society.

Pt-lanthanide metal intermetallics have been studied as alternative electrocatalysts to commercial Pt/C due to their noticeably negative heat of formation, which improves resistance to activity loss during stability tests [88–90]. Escudero-Escribano et al. introduced volcano-like relations between nearest-neighbor Pt–Pt distance ($d_{Pt\text{-}Pt}$) and H adsorption strength and ORR activity for a series of Pt_5M (M = lanthanide metal, i.e., Pt_5La, Pt_5Ce, Pt_5Sm, Pt_5Gd, Pt_5Tb, Pt_5Tm) catalysts [88]. As the dPt-Pt or lattice parameter decreases, H adsorption becomes weakened and reaches the maximum destabilization of adsorbed H for Pt_5Tb. Decreasing $d_{Pt\text{-}Pt}$, such as Pt5Tm, forms a more relaxed Pt overlayer toward more stabilized or strengthened H binding. In recent reports, the catalytic application of Pt-lanthanide metal intermetallics was extended to MOR catalysis. Zhang et al. examined Pt_5La, Pt_5Ce, Pt_5Pr, and Pt_5Nd intermetallics of hexagonal phase with P6/mmm space group show exceptional activities and stabilities in alkaline electrolyte [89]. In particular, the mass activity of Pt_5Ce (9.13 A/mg_{Pt}) exhibits a 7.4-fold enhancement relative to Pt/C (1.24 A/mg_{Pt}). After 1000 continuous potential cycles, Pt_5Ce shows a slight activity degradation of 8.4% in stark contrast to 73.8% loss for Pt/C. The electron-rich nature enables

faster electron transfer within Pt_5Ce with adequate Pt 5d-Ce 4f coupling to modulate the Pt electronic structure. Moreover, the Pt *d*-band center at a lower position away from the Fermi level leads to attenuated CO binding strength and superior CO tolerance.

The majority of Pt-based ordered intermetallic catalysts are synthesized under high temperatures, which inevitably leads to particle agglomeration and/or Ostwald ripening. Cui et al. synthesized structurally ordered Pt_3Ti and Pt_3V nanoparticles via a surfactant-free KCl-matrix approach with potassium triethylborohydride (KEt_3BH) as the strong reducing agent under air-free and aprotic-solvent (tetrahydrofuran) conditions [91]. The use of KEt_3BH is efficient in reducing the precursors of extremely oxophilic early-3d transition metals in a very fast process. KCl, generated as a by-product and insoluble in tetrahydrofuran, encapsulates the resultant intermetallic nanoparticles to suppress agglomeration during thermal annealing (Figure 7). The mass activities of Pt_3V/C and Pt_3Ti/C at 0.5 V in 0.1 M $HClO_4$ + 1 M CH_3OH are 149.4 and 200.2 mA mg_{Pt}^{-1}, respectively, significantly higher than Pt/C (53.6 mA mg_{Pt}^{-1}). The loss in current density at 0.5 V after 1000 potential cycles is 27.2% for Pt3Ti and 23.4% for Pt3V compared to 40.7% for Pt/C. This KCl-stabilization strategy was extended to the synthesis of other Pt-based ordered intermetallic catalysts. In recent years, face-centered tetragonal (*fct*) $L1_0$-phased PtCo and PtFe-ordered intermetallic catalysts with alternating Pt and Co/Fe atomic layers have become the topic of considerable research [92,93]. MgO was used to coat Pt-CoO or PtFe-Fe_3O_4 nanoparticles as an inert protective layer to keep them from aggregating during the annealing process.

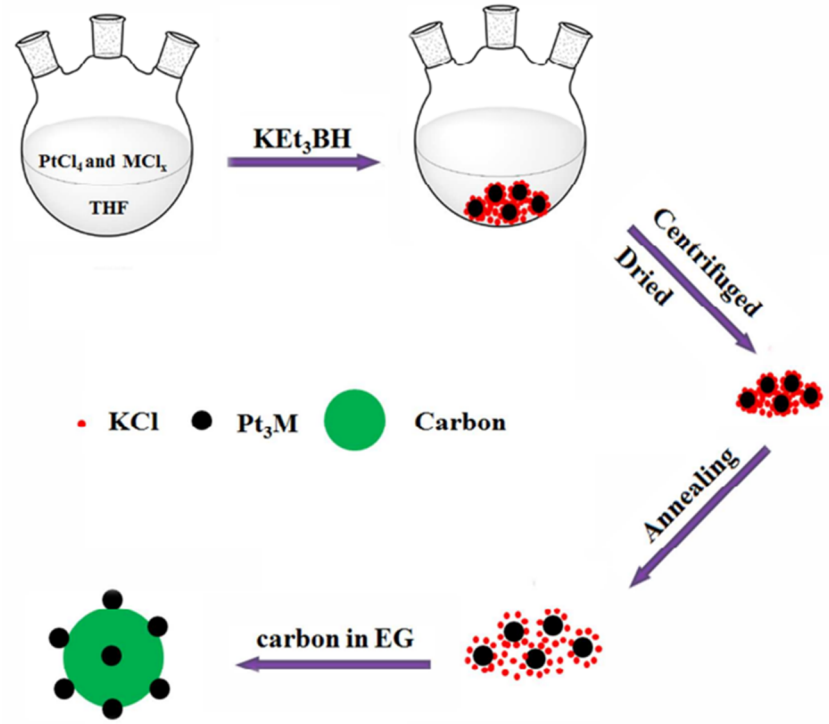

Figure 7. Schematic illustration of the synthesis of carbon-supported Pt_3Ti and Pt_3V bimetallic catalysts. Reprinted with permission from Ref. [91]. Copyright 2014, American Chemical Society.

It should be noted that in some cases, disordered alloys outperform ordered intermetallics in terms of MOR catalysis. Chen et al. conducted acetic acid and thermal treatment of the preformed ordered Pt_3Sn nanocubes to obtain well-retained ordered and disordered Pt-Sn nanocubes, respectively [71]. A higher proportion of Sn^{4+} is formed after thermal treatment because the higher mobility of Sn atoms in the thermally treated disordered nanocubes drives Sn atoms to migrate to the surface and to be oxidized. The formation of OH_{ads} due to water dissociation is promoted on Sn^{4+} sites, which facilitates CO oxidation to CO_2 on Pt sites at less positive potentials. They also demonstrated that for disordered

Pt-Sn nanocubes that undergo electrochemical activation in an alkaline electrolyte followed by MOR test by 10 cycles in an acidic electrolyte, both Sn^{4+}-to-Pt ratio and MOR-specific activity could reach the level attained by the disordered Pt-Sn nanocubes subject to electrochemical activation in an acidic electrolyte. At the same time, these properties cannot be recovered for ordered counterparts subjected to the same treatment.

5.2. Interface Engineering

The interface-driven enhancement of catalytic performances via preparing heterostructured catalysts has also been a topic of extensive research [94–98]. The interface electron transfer and redistribution is utilized to tailor the adsorption energy of reaction molecules and intermediates. By electrochemical chronoamperometric treatment of Pt_2Bi with a mixed chain-like and plate-like structure, Wang et al. synthesized a purely chain-like structure with $BiO_x(OH)_y$-Pt inverse interface [94]. The inverse interface structure is formed due to the partial leaching of Bi atoms together with anodic oxidation to Bi^{3+} in the form of $BiO_x(OH)_y$. The structural reconstruction endows the catalyst with superior CO tolerance, as evidenced by the electron deficiency of Pt, to weaken CO binding strength and to form an enhanced adsorption interaction with strongly electronegative O atoms of OH species to remove CO (Figure 8). By conjugating PtFeNi ultrathin nanowires with imidazolium-salt-based ionic liquids (ILs), Li et al. take advantage of the electronic interaction between organic coating and metallic catalysts [98]. The flexible coverage of IL layers as a shielding modulates the electronic properties of surface Pt sites via the observable e_g-t_{2g} orbital splitting of the Fe 3*d* band due to the crystal-field effect and moving of Ni 3*d* orbital closer to the Fermi level (−1.4 eV). The resultant IL/PtFeNi conjugation nanowires possess a mass activity of 1.43 A/mg_{Pt}, markedly higher than the 0.75 A/mg_{Pt} of PtFeNi nanowires and 0.36 A/mg_{Pt} of Pt/C. Tao et al. synthesized Pt/CeO2-P by Ar plasma treatment and Pt deposition for an efficient MOR catalysis [97]. The plasma irradiation of CeO_2 generates a high density of oxygen vacancies. When coupled with small Pt particle size, it promotes the transfer of surplus electrons of Pt to CeO_2 support and conversion of Ce^{4+} to Ce^{3+}. Meanwhile, the e_g-t_{2g} splitting induced by the crystal field effect serves to lower the Ce 5*d* band in energy for the Pt/CeO_2-P catalyst. The beneficial plasma treatment and strong electronic interaction at the interface endow the hybrid catalyst with a remarkable specific activity of 8.06 mA/cm^2 relative to that of Pt/CeO_2 (2.36 mA/cm^2) and Pt/C (1.72 mA/cm^2). Similarly, Chen et al. synthesized Pd nanowires decorated with crystalline CuO_x nanoparticles (Pd NW@cCuO_x) by fast air plasma treatment of Pd nanowires covered with amorphous CuOx nanolayers (Pd NW@aCuO_x) [96]. The electron-deficient $Pd^{\delta+}$ active sites with high valence states generated due to the strong Pd-O-Cu interaction at the Pd-cCuO_x interface play a key role in enhancing stability and anti-poisoning properties. With the stable Pd active sites with predominant oxidation states, the loss in MOR-specific activity after 600 potential cycles is only 20.1% for the Pd NW@cCuO_x catalyst. In contrast, the specific activity drops by 43.0% and 53.8% for Pd NW@aCuO_x and Pd NW catalysts, respectively.

5.3. Surface Facet Engineering

The selective exposure of (111) facets has been proven beneficial toward MOR catalysis with high CO tolerance because of the weakened binding strength of poisoning species such as CO_{ads} relative to other facets such as (100) [56,99–101]. Li et al. demonstrated CuNi@PtCu octahedra with (111)-terminated facets exhibit superior MOR catalytic activities compared to CuNi@PtCu polyhedra counterpart (7.49 mA cm^{-2} and 0.99 A $mg_{Pt}{}^{-1}$ vs. 5.57 mA cm^{-2} and 0.66 A $mg_{Pt}{}^{-1}$) [101]. The CuNi octahedra enclosed by (111) facets were performed, followed by Pt coating and segregation, wherein galvanic replacement between Pt and core Ni occurs to form a PtCu shell. The higher CO tolerance of CuNi@PtCu octahedra is manifested by the lower onset and peak potential of CO stripping peaks. Also, Huang et al. substantiated the (111) facet-induced advantage by preparing ultrathin PtRu nanowires enclosed by (111) facets and PtRu nanocubes enclosed by (100) facet [99].

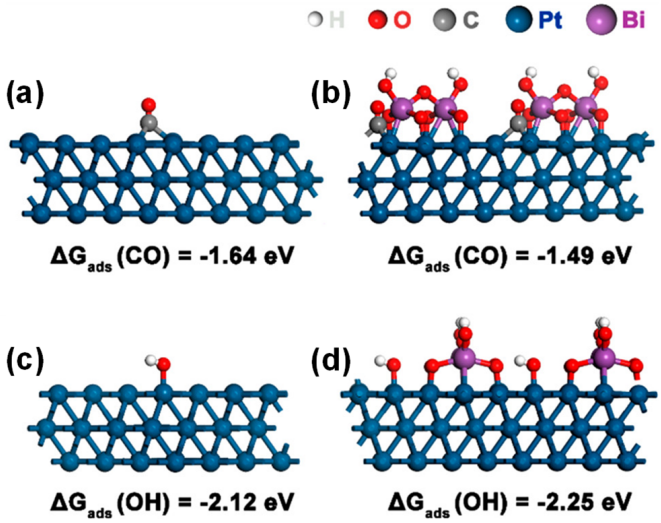

Figure 8. Theoretical calculations of CO and OH binding energies on the surfaces of (**a**,**c**) Pt(111) and (**b**,**d**) Pt(111) decorated with $BiO_x(OH)_y$. Reprinted with permission from Ref. [94]. Copyright 2020, American Chemical Society.

Due to the presence of high-density steps and lower atomic coordination numbers, Pt-based nanocrystals bounded with high-index facets (HIFs), characteristic of tetrahexahedron, trapezohedron, and trisoctahedron, possess remarkable MOR catalytic activity (Figure 9). Shen et al. showed that for an $L1_0$-Pt_1Co_1 ordered tetragonal structure, a growing portion of Bi modification can significantly reduce the specific surface energies of HIFs while increasing the specific surface energies of low-index facets (LIFs), thereby facilitating the formation of HIFs-enclosed THH alloys [102,103]. Based on this concept, A1-Pt_1Co_1 and A1-Pt_3Co_1 THH nanoparticles with the phase of solid solution were prepared via annealing at 900 °C, and $L1_0$-Pt_1Co_1 and $L1_2$-Pt_3Co_1 THH ordered intermetallic nanoparticles were obtained via subsequent annealing of the A1-phase alloy nanoparticles at 700 °C. Concerning the Pt_3Fe_1 system, the 900 °C annealing yields $L1_2$-phased THH intermetallic nanoparticles instead of an A1-phased solid solution. However, the incorporation of a third element, Ni, serves to realize L12-phased Pt3Fe0.6Ni0.4 intermetallic nanoparticles while retaining the THH structure characteristic of HIFs after annealing at a lower temperature of 600 °C. Also, their group utilized Bi shape-regulation to synthesize bimetallic, trimetallic, and tetrametallic THH alloys with heterodimer structures [104]. For instance, Pd domains and Rh domains in PdRh THH heterodimers are enclosed by high-index facets. The immiscibility between Rh and Au leads to the preferred alloying of Rh with Pt and, therefore, the formation of PtRh domains bounded by high-index facets and Au-alone domains bounded by low-index facets as Rh is incorporated into PtAu heterodimers. By using the seed-mediated approach, Song et al. synthesized hyperbranched trisoctahedral core–shell (HTCS) Au@PdPt catalysts based on preformed trisoctahedral Au cores bounded by (331) facets [105]. The conformal growth of the outermost PdPt shell retains the trisoctahedral morphology. The HTCS Au@PdPt catalysts show mass activity and specific activity of 0.64 A mg_{Pt}^{-1} and 1.16 mA cm^{-2}, respectively, enhanced relative to Au@PdPt catalysts with spherical Au cores (0.36 A mg_{Pt}^{-1} and 0.71 mA cm^{-2}) and octahedral cores (0.42 A mg_{Pt}^{-1} and 0.80 mA cm^{-2}).

A concave nanocube formed from kinetically controlled growth represents a classic form of nanocrystal enclosed by HIFs. The identification of these facets with {hk0} orientation involves measuring the angle between {hk0} and {100} facets observed in the corresponding high-resolution transmission electron microscopy images [106]. Li et al. investigated the effect of Sn doping into Pt_3Mn concave nanocubes with HIFs [107]. The Sn doping gives rise to surface alloying of the three constituent elements without destroying the HIFs-bounded structure. More importantly, Sn doping provides stabilization to

the surface structure with negligible morphological change after 2000 potential cycles of stability test. The retention of MOR activities after 2000 cycles reach as high as 65.7% for 0.5%/Pt_3Mn relative to 42.3% for undoped Pt_3Mn and 5.5% for Pt/C. Apart from doping-induced stabilization, some reports demonstrated anisotropic nanowires that serve to relieve the high surface energy intrinsic to HIFs while guaranteeing intimate contact with carbon supports. Luo et al. synthesized a zigzag-like PtFe anisotropic nanowire with a two-atomic-layer Pt skin [108]. The product exhibits a mass activity of 3.34 A/mg_{Pt} with substantial improvement relative to Pt/C (0.70 A/mg_{Pt}). The current density retention of 35.7% after the chronoamperometric test of 5000s is also much higher than that of Pt/C (9.6%).

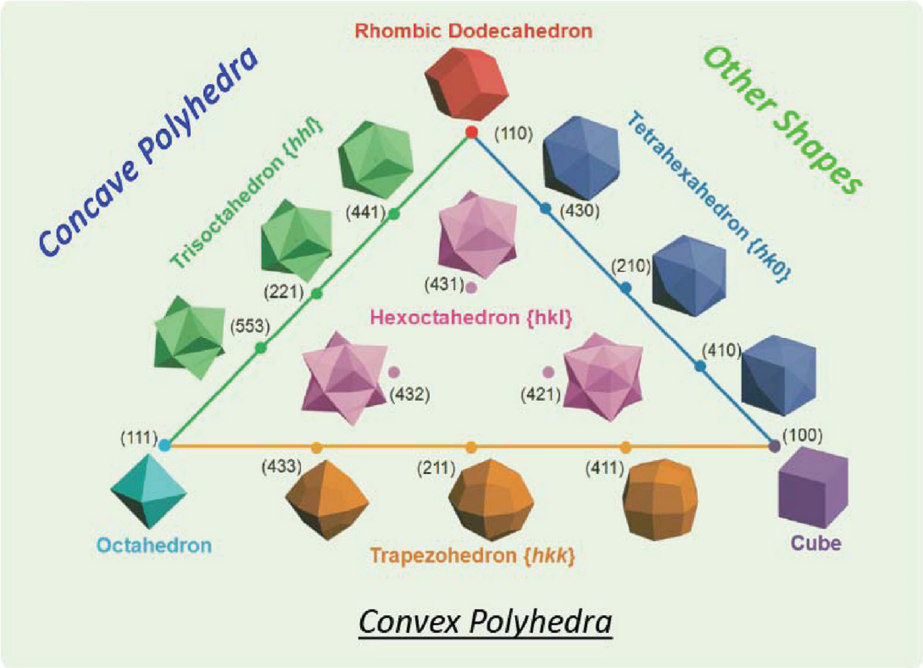

Figure 9. Polyhedral nanocrystals enclosed by high-index crystalline facets based on low-index facet featured structures. Reprinted with permission from Ref. [109]. Copyright 2013, American Chemical Society.

6. The Use of High-Entropy Alloys in Electrocatalysis

High-entropy alloys (HEAs), a unique class of multimetallic alloys with five or more elemental components, have become a hot research topic in the past few years. The varied elemental composition enables the infinite tuning possibility of adsorption energies toward intermediate species, thereby promoting electrocatalytic activity, selectivity, and stability. A growing portion of reports are being focused on the electrocatalytic application of HEAs on oxygen reduction reaction, methanol oxidation reaction, hydrogen evolution reaction, oxygen evolution reaction, etc. [34,83,110–114]. The mixed configuration entropy (S) reaches more than 1.5 R (wherein R denotes molar gas constant) at a homogeneous atomic percentage of 5~35% for each element [115,116]. In addition to the high-entropy effect, the lattice distortion effect due to the variation of the atomic size of each elemental component in HEAs and the sluggish diffusion effect due to the high diffusion energy barrier of elemental components contribute to modulating the electronic structure and enhancing thermal stability.

Chen et al. synthesized PtRhBiSnSb high-entropy intermetallic (HEI) nanoplates with distinct hexagonal close-packed (hcp) crystalline structure [83]. The partial substitution of Pt atoms by Rh atoms and Bi atoms by Sn/Sb atoms leads to not only efficient electron transfer via p-d orbital hybridization but also robust valence states. The reaction energy diagrams, in conjunction with in situ infrared spectra, reveal the strong preference

toward non-CO HCOOH ($HCOO_{ads}$) pathway by PtRhBiSnSb HEI nanoplates. Zhao et al. employed a distinct approach of spray drying (SD) and thermal decomposition reduction (TDR) to fabricate a class of high-entropy alloy nanoparticles with a single phase of solid solution [117]. The SD process involves the rapid formation of dry precursor nanoparticles in less than 0.6 seconds in the drying chamber after the solution precursor emerges from the nozzle in less than 0.00017 seconds. The TDR process includes thermal nucleation and nanocrystal growth, which involves the three stages of aggregation and coalescence, oriented attachment, and Ostwald ripening. In addition, the abundant hydrogen bonds between the precursor solution and oxygenated groups on the GO substrate help to anchor as-formed precursor nanoparticles. The resultant senary PtCoCuRuNiFe HEA nanoparticles supported on rGO possess mass activity of 1.51 A mg_{Pt}^{-1} compared to that of Pt/C (0.3 A mg_{Pt}^{-1}) in 0.5 M H_2SO_4 + 0.5 M CH_3OH electrolyte. Li et al. fabricated $Pt_{18}Ni_{26}Fe_{15}Co_{14}Cu_{27}$ high-entropy alloy nanoparticles by a simple oleylamine-based oil-phase approach (Figure 10) [33]. They exhibit remarkable alkaline MOR activity (15.04 A $mg^{-1}{}_{Pt}$) and anti-CO poisoning properties in 1 M KOH + 1 M CH_3OH. After 1000 CV cycles, the MOR activity of $Pt_{18}Ni_{26}Fe_{15}Co_{14}Cu_{27}$ declines by only 6.4%, in sharp contrast to 26.9% for Pt/C. The electron transfer is markedly promoted for MOR catalysis, wherein the lowest location of Pt-5*d* serves as an electron reservoir while Ni-3*d* and Co-3*d* with high-lying positions serve as electron depletion centers. The 3*d* orbitals of Cu, Co, and Fe mitigate the energy barrier for MOR electron transfer. Moreover, the linear relation for energy positions of *s*,*p* orbitals of MOR intermediates (CH_3O*, CH_2O*, CHO*, CO_2) gives rise to optimal binding strength and thus exceptional MOR catalytic activity of PtNiFeCoCu high-entropy alloy nanoparticles. Using a compressive strain engineering strategy, Wang et al. synthesized PtFeCoNiCu HEA nanoparticles with face-centered cubic structures by calcination of the precursor at 400 °C (HEA-400) and 700 °C (HEA-700) [118]. The 0.94% compressive strain, as evidenced by the shortened Pt–Pt bond length of HEA-700 compared to HEA-400, promotes the CO tolerance of the former catalyst. The HEA-700 and HEA-400 exhibit MOR mass activities of 1.40 A mg_{Pt}^{-1} and 1.30 A mg_{Pt}^{-1}, respectively, 2.50 and 2.32 times higher than that of Pt/C. The peak current density ratios of forward to backward (I_f/I_b) are 1.21, 1.09, and 0.58 for HEA-700, HEA-400, and Pt/C, respectively. The downshift of the *d*-band center in HEA-700 corroborates its weaker CO adsorption and remarkable MOR activity.

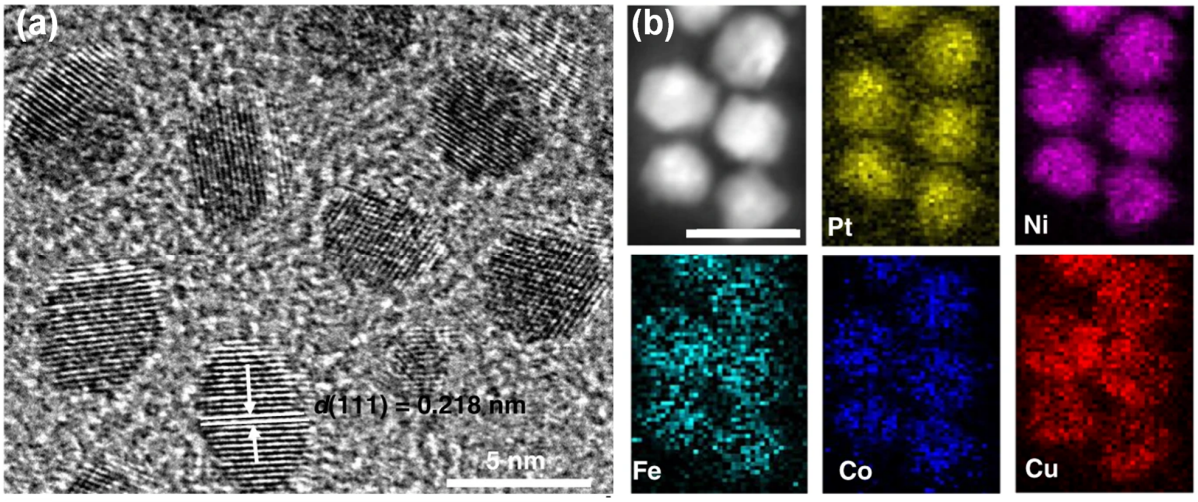

Figure 10. *Cont.*

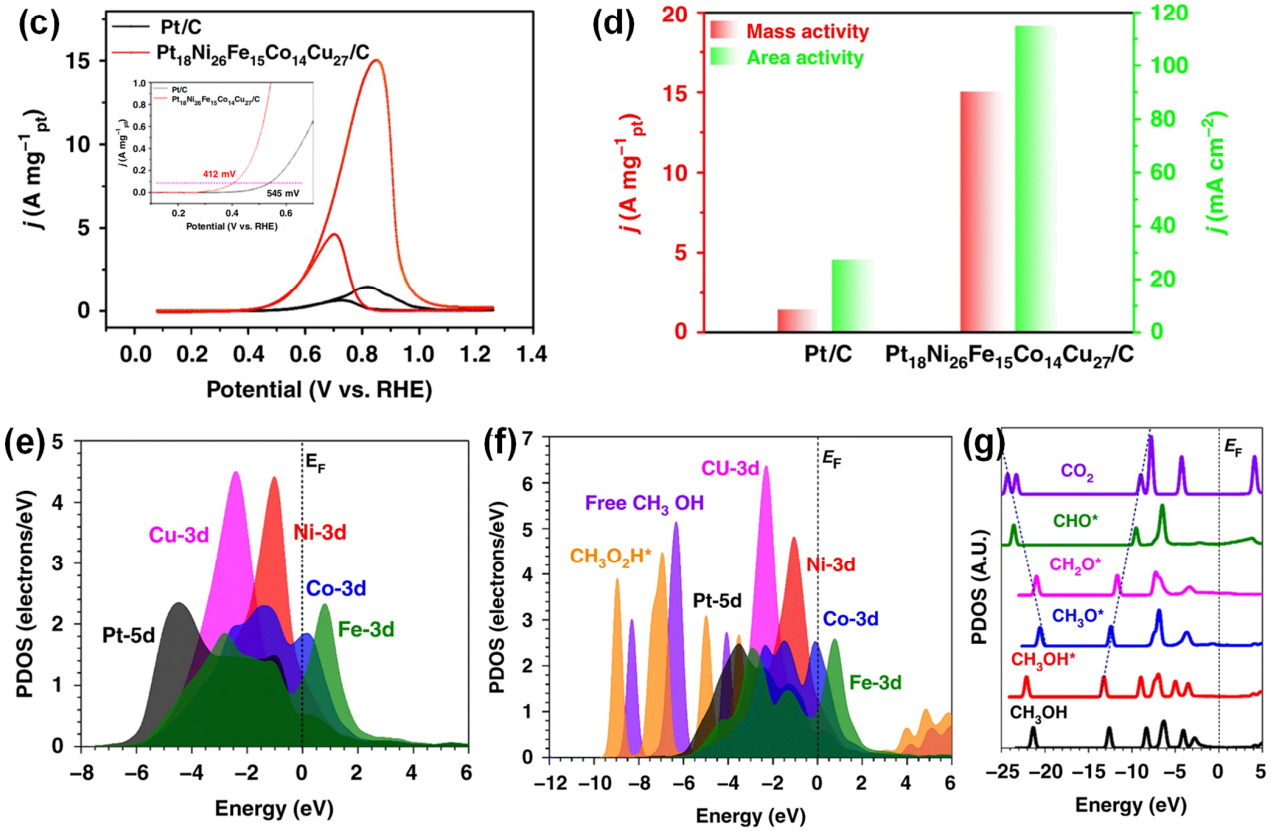

Figure 10. (**a**) High-resolution TEM image of $Pt_{18}Ni_{26}Fe_{15}Co_{14}Cu_{27}$ nanoparticles. (**b**) Corresponding elemental mapping profiles. (**c**) MOR CVs and (**d**) activity histograms of $Pt_{18}Ni_{26}Fe_{15}Co_{14}Cu_{27}/C$ and Pt/C in 1 M KOH + 1 M CH_3OH. (**e**) The PDOSs of $Pt_{18}Ni_{26}Fe_{15}Co_{14}Cu_{27}$ nanoparticles. The PDOSs of (**f**) CH_3OH adsorption and (**g**) MOR key intermediates. Reprinted with permission from Ref. [33]. Copyright 2020, Nature Publishing Group.

7. Conclusions and Perspectives

The MOR kinetics determines the overall anodic performance of direct methanol fuel cells. Based on classic *d*-band theory, a wide variety of MOR catalysts have been developed with exceptional catalytic activity, CO tolerance and stability (Table 1). The formation of intermetallic compounds serves to modulate electronic structure via ligand effect and strain effect. Interfacial electronic engineering and surface facet engineering can also be employed to tune the chemisorption of reaction intermediates. These strategies are usually combined or jointly function when it comes to designing highly effective MOR catalysts.

Table 1. Comparison of recently reported catalysts, mass and specific activities, and stabilities.

Catalysts	Electrolyte	Mass Activity (A $mg_{Pt/Pd}{}^{-1}$)	Specific Activity (mA cm^{-2})	Stability (Retention in Activity after Tests	References
22% YO_x/MoO_x-Pt ultrathin nanowires	0.1 M $HClO_4$ + 0.5 M CH_3OH	2.10	3.25	64.7% after 1200 cycles (Pt/C: 50.6%)	[1]
$Pt_{69}Ni_{16}Rh_{15}$ ultrathin nanowires	0.1 M $HClO_4$ + 0.5 M CH_3OH	1.72	2.49	146.8 mA $mg_{Pt}{}^{-1}$ after 5000 s (Pt/C: 17.2 mA $mg_{Pt}{}^{-1}$)	[4]
screw thread-like $PtCu_{2.1}$ nanowires	0.1 M $HClO_4$ + 0.2 M CH_3OH	1.56	3.31	72.9% after 1000 cycles (Pt/C: 27.6%)	[119]
$Pt_{77}Co_{11}Rh_{12}$ spiral nanowires	0.1 M $HClO_4$ + 0.5 M CH_3OH	1.48	4.76	74.3% after 1600 cycles (Pt/C: 49.9%)	[120]

Table 1. *Cont.*

Pt_2Bi nanochains	1 M KOH + 1 M CH_3OH	4.61	N/A	1.52 A mg_{Pt}^{-1} after 10,000 s (Pt/C: 0.28 A mg_{Pt}^{-1})	[94]
Pt_3Bi_3Zn nanoplates	0.1 M $HClO_4$ + 0.5 M CH_3OH	3.29	3.02	71% after 1000 cycles (Pt/C: 58%)	[2]
$Pt_{94}Zn_6$ zigzag-like nanowires	0.1 M $HClO_4$ + 0.2 M CH_3OH	0.51	2.98	~60 mA mg_{Pt}^{-1} after 3000 s (Pt/C: ~8 mA mg_{Pt}^{-1})	[121]
$Pd_{59}Fe_{27}Pt_{14}$ nanomeshes	0.1 M $HClO_4$ + 0.5 M CH_3OH	1.61	4.36	80% after 500 cycles (Pt/C: 40%)	[36]
PtCoNiRh ultrathin nanowires	0.1 M $HClO_4$ + 0.5 M CH_3OH	1.36	2.08	~0.30 A mg_{Pt}^{-1} after 10,000 s (Pt/C: ~0.08 A mg_{Pt}^{-1})	[20]
$Pt_{18}Ni_{26}Fe_{15}Co_{14}Cu_{27}$ high-entropy alloy nanoparticles	1 M KOH + 1 M CH_3OH	15.04	114.93	93.6% after 1000 cycles (Pt/C: 73.1%)	[33]
PtBi@6.7%Pb nanoplates	1 M KOH + 1 M CH_3OH	13.93	43.32	71.9% after 3000 cycles	[74]
PtPb/C irra-3 nanoplates	0.1 M $HClO_4$ + 0.1 M CH_3OH	5.15	6.22	52.4% after 2500 cycles (Pt/C: 18.2%)	[122]
$Pt_{64}Fe_{20}Ir_{16}$ jagged nanowires	0.1 M $HClO_4$ + 0.5 M CH_3OH	2.13	4.25	1.34 A mg_{Pt}^{-1} after 10,000 s (Pt/C: 0.30 A mg_{Pt}^{-1})	[26]
$Pt_{62}Ru_{18}Ni_{20}$–O ultrathin nanowires	0.5 M H_2SO_4 + 0.5 M CH_3OH	2.72	4.36	92.4% after 1000 cycles (Pt/C: 79.8%)	[6]
core-shell $Pt_{56}Cu_{28}Ni_{16}$ tetrahedra	1 M KOH + 1 M CH_3OH	7.0	14.0	0.83 A mg_{Pt}^{-1} after 3600 s (Pt/C: 0.20 A mg_{Pt}^{-1})	[123]

There are still some issues in need of being addressed. First, most Pt-based alloys possess conventional *fcc* or ordered *fct* phases. Novel crystal phases with tailorable morphologies may boost catalytic performances. Second, mixed-dimensional structured Pt alloys may be beneficial to MOR catalysis via the synergistic effect of individual components and interfacial engineering. Third, a precisely controlled structure of high-entropy alloy to better expose active centers and tune their composition may represent a promising research direction. Last but not least, efficient MOR catalysts need to be assessed under DMFC operating conditions for practical applications, even if fuel cell performances are affected by many factors, such as ionomer-to-catalyst weight ratio. Maya-Cornejo et al. discovered that $Pt_{67}Ru_{33}$ alloy supported on single-wall carbon nanotubes (SWCNT) reaches a peak power density of 132 mW cm^{-2} at a Pt loading of 1.0 mg cm^{-2} [124]. Wang et al. measured DMFC performances of the membrane electrode assemblies (MEAs) based on dealloyed PtCu with Cu-vacancies (d-Pt_2Cu_1 NWs) as anode catalyst and commercial Pt/C as cathode catalyst [3]. At a low Pt loading of 0.6 mg, the d-PtCu NWs catalyst layer with 12 wt% ionomer at 80 °C achieved a peak power density of 49.3 mW cm^{-2}. The MEAs show ~94% activity retention after 24 h at the current density of 50 mA cm^{-2}. All in all, Pt-based alloys show favorable prospects for DMFC systems.

Author Contributions: R.Y.: Investigation, Conceptualization, Formal analysis, Writing of the original draft. Y.Z. (Yifan Zhang): Conceptualization, Formal analysis, Writing of the original draft. S.D.: Conceptualization, Formal analysis. R.Z.: Formal analysis. S.Z.: Formal analysis. J.Z.: Formal Analysis. Y.Z. (Yufeng Zhao): Supervision, Funding acquisition, Formal Analysis. Z.X.: Supervision, Conceptualization, Formal Analysis, Writing and editing of the final draft. All authors have read and agreed to the published version of the manuscript.

Funding: This work was financially supported by the Shanghai University–Chaowei Group (Zhejiang) Joint Laboratory Program (18H01928) and the Natural Science Foundation in Shanghai (21ZR1424200).

Conflicts of Interest: The authors declare no conflicts of interest.

References

1. Li, M.; Zhao, Z.; Zhang, W.; Luo, M.; Tao, L.; Sun, Y.; Xia, Z.; Chao, Y.; Yin, K.; Zhang, Q.; et al. Sub-monolayer YOx/MoOx on ultrathin Pt nanowires boosts alcohol oxidation electrocatalysis. *Adv. Mater.* **2021**, *33*, 2103762. [CrossRef] [PubMed]
2. Tian, H.; Wu, D.; Li, J.; Luo, J.; Jia, C.; Liu, Z.; Huang, W.; Chen, Q.; Shim, C.M.; Deng, P.; et al. Rational design ternary platinum based electrocatalysts for effective methanol oxidation reaction. *J. Energy Chem.* **2022**, *70*, 230–235. [CrossRef]
3. Wang, K.; Huang, D.; Guan, Y.; Liu, F.; He, J.; Ding, Y. Fine-tuning the electronic structure of dealloyed PtCu nanowires for efficient methanol oxidation reaction. *ACS Catal.* **2021**, *11*, 14428–14438. [CrossRef]
4. Zhang, W.; Yang, Y.; Huang, B.; Lv, F.; Wang, K.; Li, N.; Luo, M.; Chao, Y.; Li, Y.; Sun, Y.; et al. Ultrathin PtNiM (M = Rh, Os, and Ir) nanowires as efficient fuel oxidation electrocatalytic materials. *Adv. Mater.* **2019**, *31*, e1805833. [CrossRef] [PubMed]
5. Lamy, C.; Léger, J.-M.; Srinivasan, S. Direct methanol fuel cells: From a twentieth century electrochemist's dream to a twenty-first century emerging technology. In *Modern Aspects of Electrochemistry*; Bockris, J.O.M., Conway, B.E., White, R.E., Eds.; Kluwer Academic Publishers: New York, NY, USA, 2002; pp. 53–118.
6. Li, H.; Pan, Y.; Zhang, D.; Han, Y.; Wang, Z.; Qin, Y.; Lin, S.; Wu, X.; Zhao, H.; Lai, J.; et al. Surface oxygen-mediated ultrathin PtRuM (Ni, Fe, and Co) nanowires boosting methanol oxidation reaction. *J. Mater. Chem. A* **2019**, *8*, 2323–2330. [CrossRef]
7. Sheng, T.; Ma, Z.-W.; Sun, S.-G. Insights into the Pt/Rh(1 1 1) interface for direct ethanol fuel cells. *Appl. Surf. Sci.* **2020**, *502*, 144093. [CrossRef]
8. Sheng, T.; Sun, S.-G. Insight into the promoting role of Rh doped on Pt(111) in methanol electro-oxidation. *J. Electroanal. Chem.* **2016**, *781*, 24–29. [CrossRef]
9. Belenov, S.; Pavlets, A.; Paperzh, K.; Mauer, D.; Menshikov, V.; Alekseenko, A.; Pankov, I.; Tolstunov, M.; Guterman, V. The PtM/C (M = Co, Ni, Cu, Ru) electrocatalysts: Their synthesis, structure, activity in the oxygen reduction and methanol oxidation reactions, and durability. *Catalysts* **2023**, *13*, 243. [CrossRef]
10. Deshpande, P.; Prasad, B.L.V. Alloying with Mn enhances the activity and durability of the CoPt catalyst toward the methanol oxidation reaction. *ACS Appl. Mater. Interfaces* **2023**, *15*, 26554–26562. [CrossRef]
11. Kwon, T.; Jun, M.; Kim, H.Y.; Oh, A.; Park, J.; Baik, H.; Joo, S.H.; Lee, K. Vertex-reinforced PtCuCo ternary nanoframes as efficient and stable electrocatalysts for the oxygen reduction reaction and the methanol oxidation reaction. *Adv. Funct. Mater.* **2018**, *28*, 1706440. [CrossRef]
12. Pramadewandaru, R.K.; Lee, Y.W.; Hong, J.W. Synergistic effect of bimetallic Pd-Pt nanocrystals for highly efficient methanol oxidation electrocatalysts. *RSC Adv.* **2023**, *13*, 27046–27053. [CrossRef] [PubMed]
13. Roessner, L.; Armbruester, M. Electrochemical energy conversion on intermetallic compounds: A review. *ACS Catal.* **2019**, *9*, 2018–2062. [CrossRef]
14. Casado-Rivera, E.; Volpe, D.J.; Alden, L.; Lind, C.; Downie, C.; Vázquez-Alvarez, T.; Angelo, A.C.D.; DiSalvo, F.J.; Abruña, H.D. Electrocatalytic activity of ordered intermetallic phases for fuel cell applications. *J. Am. Chem. Soc.* **2004**, *126*, 4043–4049. [CrossRef] [PubMed]
15. Ghosh, T.; Leonard, B.M.; Zhou, Q.; DiSalvo, F.J. Pt alloy and intermetallic phases with V, Cr, Mn, Ni, and Cu: Synthesis as nanomaterials and possible applications as fuel cell catalysts. *Chem. Mater.* **2010**, *22*, 2190–2202. [CrossRef]
16. Oezaslan, M.; Hasché, F.; Strasser, P. Pt-based core-shell catalyst architectures for oxygen fuel cell electrodes. *J. Phys. Chem. Lett.* **2013**, *4*, 3273–3291. [CrossRef]
17. Strasser, P.; Koh, S.; Anniyev, T.; Greeley, J.; More, K.; Yu, C.; Liu, Z.; Kaya, S.; Nordlund, D.; Ogasawara, H.; et al. Lattice-strain control of the activity in dealloyed core-shell fuel cell catalysts. *Nat. Chem.* **2010**, *2*, 454–460. [CrossRef] [PubMed]
18. Kuttiyiel, K.A.; Sasaki, K.; Choi, Y.; Su, D.; Liu, P.; Adzic, R.R. Bimetallic IrNi core platinum monolayer shell electrocatalysts for the oxygen reduction reaction. *Energy Environ. Sci.* **2012**, *5*, 5297–5304. [CrossRef]
19. Norskov, J.K.; Abild-Pedersen, F.; Studt, F.; Bligaard, T. Density functional theory in surface chemistry and catalysis. *Proc. Natl. Acad. Sci. USA* **2011**, *108*, 937–943. [CrossRef]
20. Wang, W.; Chen, X.; Zhang, X.; Ye, J.; Xue, F.; Zhen, C.; Liao, X.; Li, H.; Li, P.; Liu, M.; et al. Quatermetallic Pt-based ultrathin nanowires intensified by Rh enable highly active and robust electrocatalysts for methanol oxidation. *Nano Energy* **2020**, *71*, 104623. [CrossRef]
21. Tang, J.-X.; Chen, Q.-S.; You, L.-X.; Liao, H.-G.; Sun, S.-G.; Zhou, S.-G.; Xu, Z.-N.; Chen, Y.-M.; Guo, G.-C. Screw-like PdPt nanowires as highly efficient electrocatalysts for methanol and ethylene glycol oxidation. *J. Mater. Chem. A* **2018**, *6*, 2327–2336. [CrossRef]
22. Zhao, F.; Ye, J.; Yuan, Q.; Yang, X.; Zhou, Z. Realizing a CO-free pathway and enhanced durability in highly dispersed Cu-doped PtBi nanoalloys towards methanol full electrooxidation. *J. Mater. Chem. A* **2020**, *8*, 11564–11572. [CrossRef]
23. Zhu, R.; Yu, Y.; Yu, R.; Lai, J.; Jung, J.C.-Y.; Zhang, S.; Zhao, Y.; Zhang, J.; Xia, Z. PtIrM (M = Ni, Co) jagged nanowires for efficient methanol oxidation electrocatalysis. *J. Colloid Interface Sci.* **2022**, *625*, 493–501. [CrossRef] [PubMed]
24. Qi, Z.; Xiao, C.; Liu, C.; Goh, T.W.; Zhou, L.; Maligal-Ganesh, R.V.; Pei, Y.; Li, X.; Curtiss, L.A.; Huang, W. Sub-4 nm PtZn intermetallic nanoparticles for enhanced mass and specific activities in catalytic electrooxidation reaction. *J. Am. Chem. Soc.* **2017**, *139*, 4762–4768. [CrossRef] [PubMed]
25. Wang, X.; Liu, Y.; Ma, X.-Y.; Chang, L.-Y.; Zhong, Q.; Pan, Q.; Wang, Z.; Yuan, X.; Cao, M.; Lyu, F.; et al. The Role of Bismuth in Suppressing the CO Poisoning in Alkaline Methanol Electrooxidation: Switching the Reaction from the CO to Formate Pathway. *Nano Lett.* **2023**, *23*, 685–693. [CrossRef] [PubMed]

26. Zhu, R.; Yu, R.; Yin, K.; Zhang, S.; Jung, J.C.-Y.; Zhao, Y.; Li, M.; Xia, Z.; Zhang, J. Integration of multiple advantages into one catalyst: Non-CO pathway of methanol oxidation electrocatalysis on surface Ir-modulated PtFeIr jagged nanowires. *J. Colloid Interface Sci.* **2023**, *640*, 348–358. [CrossRef]
27. Zeng, R.; Yang, Y.; Shen, T.; Wang, H.; Xiong, Y.; Zhu, J.; Wang, D.; Abruña, H.D. Methanol oxidation using ternary ordered intermetallic electrocatalysts: A DEMS study. *ACS Catal.* **2020**, *10*, 770–776. [CrossRef]
28. Kitchin, J.R.; Nørskov, J.K.; Barteau, M.A.; Chen, J.G. Role of strain and ligand effects in the modification of the electronic and chemical properties of bimetallic surfaces. *Phys. Rev. Lett.* **2004**, *93*, 156801. [CrossRef]
29. Mavrikakis, M.; Hammer, B.; Nørskov, J.K. Effect of strain on the reactivity of metal surfaces. *Phys. Rev. Lett.* **1998**, *81*, 2819–2822. [CrossRef]
30. Stamenkovic, V.; Mun, B.S.; Mayrhofer, K.J.J.; Ross, P.N.; Markovic, N.M.; Rossmeisl, J.; Greeley, J.; Nørskov, J.K. Changing the activity of electrocatalysts for oxygen reduction by tuning the surface electronic structure. *Angew. Chem. Int. Ed.* **2006**, *45*, 2897–2901. [CrossRef]
31. Nilsson, A.; Pettersson, L.G.M.; Hammer, B.; Bligaard, T.; Christensen, C.H.; Nørskov, J.K. The electronic structure effect in heterogeneous catalysis. *Catal. Lett.* **2005**, *100*, 111–114. [CrossRef]
32. Ruban, A.; Hammer, B.; Stoltze, P.; Skriver, H.; Nørskov, J. Surface electronic structure and reactivity of transition and noble metals. *J. Mol. Catal. A Chem.* **1997**, *115*, 421–429. [CrossRef]
33. Li, H.; Han, Y.; Zhao, H.; Qi, W.; Zhang, D.; Yu, Y.; Cai, W.; Li, S.; Lai, J.; Huang, B.; et al. Fast site-to-site electron transfer of high-entropy alloy nanocatalyst driving redox electrocatalysis. *Nat. Commun.* **2020**, *11*, 5437. [CrossRef]
34. Li, H.; Sun, M.; Pan, Y.; Xiong, J.; Feng, S.; Li, Z.; Lai, J.; Huang, B.; Wang, L. The self-complementary effect through strong orbital coupling in ultrathin high-entropy alloy nanowires boosting pH-universal multifunctional electrocatalysis. *Appl. Catal. B Environ.* **2022**, *312*, 121431. [CrossRef]
35. Zhan, C.; Xu, Y.; Bu, L.; Zhu, H.; Feng, Y.; Yang, T.; Zhang, Y.; Yang, Z.; Huang, B.; Shao, Q.; et al. Subnanometer high-entropy alloy nanowires enable remarkable hydrogen oxidation catalysis. *Nat. Commun.* **2021**, *12*, 6261. [CrossRef] [PubMed]
36. Luo, X.; Liu, C.; Wang, X.; Shao, Q.; Pi, Y.; Zhu, T.; Li, Y.; Huang, X. Spin regulation on 2D Pd-Fe-Pt nanomeshes promotes fuel electrooxidations. *Nano Lett.* **2020**, *20*, 1967–1973. [CrossRef]
37. Zhang, Y.; Huang, B.; Shao, Q.; Feng, Y.; Xiong, L.; Peng, Y.; Huang, X. Defect engineering of palladium-tin nanowires enables efficient electrocatalysts for fuel cell reactions. *Nano Lett.* **2019**, *19*, 6894–6903. [CrossRef] [PubMed]
38. Qin, Y.; Huang, H.; Yu, W.; Zhang, H.; Li, Z.; Wang, Z.; Lai, J.; Wang, L.; Feng, S. Porous PdWM (M = Nb, Mo and Ta) trimetallene for high C1 selectivity in alkaline ethanol oxidation reaction. *Adv. Sci.* **2022**, *9*, 2103722. [CrossRef]
39. Wang, H.; Liang, Y.; Liu, S.; Yu, H.; Deng, K.; Xu, Y.; Li, X.; Wang, Z.; Wang, L. Electron regulation of heterostructured Pt/Rh metallene boosts ethylene glycol electrooxidation and hydrogen evolution. *Inorg. Chem.* **2023**, *62*, 14477–14483. [CrossRef]
40. Wang, H.; Wang, W.; Mao, Q.; Yu, H.; Deng, K.; Xu, Y.; Li, X.; Wang, Z.; Wang, L. Tensile strained PdNi bimetallene for energy-efficient hydrogen production integrated with formate oxidation. *Chem. Eng. J.* **2022**, *450*, 137995. [CrossRef]
41. Xiong, J.; Li, H.; Pan, Y.; Liu, J.; Zhang, Y.; Xu, J.; Li, B.; Lai, J.; Wang, L. Multiple strategies of porous tetrametallene for efficient ethanol electrooxidation. *J. Mater. Chem. A* **2022**, *10*, 23015–23022. [CrossRef]
42. Zhao, Y.; Yuan, Z.-H.; Huang, J.-T.; Wang, M.-Y.; He, B.; Ding, Y.; Jin, P.-J.; Chen, Y. Rhodium metallene-supported platinum nanocrystals for ethylene glycol oxidation reaction. *Nanoscale* **2023**, *15*, 1947–1952. [CrossRef] [PubMed]
43. Luo, M.; Zhao, Z.; Zhang, Y.; Sun, Y.; Xing, Y.; Lv, F.; Yang, Y.; Zhang, X.; Hwang, S.; Qin, Y.; et al. PdMo bimetallene for oxygen reduction catalysis. *Nature* **2019**, *574*, 81–85. [CrossRef]
44. Wang, H.; Li, Y.; Liu, S.; Yu, H.; Deng, K.; Wang, Z.; Xu, Y.; Wang, L. B-Doping-Induced Lattice Expansion of Pd Metallene Nanoribbons for Oxygen Reduction Reaction. *Inorg. Chem.* **2023**, *62*, 15157–15163. [CrossRef] [PubMed]
45. Wang, Z.; Tian, P.; Zhang, H.; Deng, K.; Yu, H.; Xu, Y.; Li, X.; Wang, H.; Wang, L. PdCu bimetallene for enhanced oxygen reduction electrocatalysis. *Inorg. Chem.* **2023**, *62*, 5622–5629. [CrossRef] [PubMed]
46. Wang, Z.; Xu, S.; Mao, Q.; Deng, K.; Xu, Y.; Wang, H.; Yu, H.; Wang, L. Polyethylenimine-ethylenediamine-induced Pd metallene toward alkaline oxygen reduction. *Inorg. Chem.* **2023**, *62*, 13537–13543. [CrossRef] [PubMed]
47. Yu, H.; Zhou, T.; Wang, Z.; Xu, Y.; Li, X.; Wang, L.; Wang, H. Defect-rich porous palladium metallene for enhanced alkaline oxygen reduction electrocatalysis. *Angew. Chem.-Int. Ed.* **2021**, *60*, 12027–12031. [CrossRef] [PubMed]
48. Zhang, H.; Li, X.; Wang, Y.; Deng, K.; Yu, H.; Xu, Y.; Wang, H.; Wang, Z.; Wang, L. Porous PdZn bimetallene for oxygen reduction electrolysis. *Appl. Catal. B Environ.* **2023**, *338*, 123006. [CrossRef]
49. Wu, J.; Cui, X.; Fan, J.; Zhao, J.; Zhang, Q.; Jia, G.; Wu, Q.; Zhang, D.; Hou, C.; Xu, S.; et al. Stable bimetallene hydride boosts anodic CO tolerance of fuel cells. *ACS Energy Lett.* **2021**, *6*, 1912–1919. [CrossRef]
50. Feng, Y.; Zhao, Z.; Li, F.; Bu, L.; Shao, Q.; Li, L.; Wu, J.; Zhu, X.; Lu, G.; Huang, X. Highly surface-distorted Pt superstructures for multifunctional electrocatalysis. *Nano Lett.* **2021**, *21*, 5075–5082. [CrossRef]
51. Gong, W.; Jiang, Z.; Wu, R.; Liu, Y.; Huang, L.; Hu, N.; Tsiakaras, P.; Shen, P.K. Cross-double dumbbell-like Pt-Ni nanostructures with enhanced catalytic performance toward the reactions of oxygen reduction and methanol oxidation. *Appl. Catal. B Environ.* **2019**, *246*, 277–283. [CrossRef]
52. Liang, W.; Wang, Y.; Zhao, L.; Guo, W.; Li, D.; Qin, W.; Wu, H.; Sun, Y.; Jiang, L. 3D anisotropic Au@Pt-Pd hemispherical nanostructures as efficient electrocatalysts for methanol, ethanol, and formic acid oxidation reaction. *Adv. Mater.* **2021**, *33*, 2100713. [CrossRef] [PubMed]

53. Shang, C.; Guo, Y.; Wang, E. Ultrathin nanodendrite surrounded PtRuNi nanoframes as efficient catalysts for methanol electrooxidation. *J. Mater. Chem. A* **2019**, *7*, 2547–2552. [CrossRef]
54. Wang, Z.; Huang, L.; Tian, Z.Q.; Shen, P.K. The controllable growth of PtCuRh rhombic dodecahedral nanoframes as efficient catalysts for alcohol electrochemical oxidation. *J. Mater. Chem. A* **2019**, *7*, 18619–18625. [CrossRef]
55. Xia, T.; Zhao, K.; Zhu, Y.; Bai, X.; Gao, H.; Wang, Z.; Gong, Y.; Feng, M.; Li, S.; Zheng, Q.; et al. Mixed-dimensional Pt-Ni alloy polyhedral nanochains as bifunctional electrocatalysts for direct methanol fuel cells. *Adv. Mater.* **2023**, *35*, e2206508. [CrossRef] [PubMed]
56. Xiao, Y.-X.; Ying, J.; Tian, G.; Yang, X.; Zhang, Y.-X.; Chen, J.-B.; Wang, Y.; Symes, M.D.; Ozoemena, K.I.; Wu, J.; et al. Hierarchically Fractal PtPdCu Sponges and their Directed Mass- and Electron-Transfer Effects. *Nano Lett.* **2021**, *21*, 7870–7878. [CrossRef] [PubMed]
57. Yao, W.; Jiang, X.; Li, M.; Li, Y.; Liu, Y.; Zhan, X.; Fu, G.; Tang, Y. Engineering hollow porous platinum-silver double-shelled nanocages for efficient electro-oxidation of methanol. *Appl. Catal. B Environ.* **2021**, *282*, 119595. [CrossRef]
58. Zhang, J.; Li, H.; Ye, J.; Cao, Z.; Chen, J.; Kuang, Q.; Zheng, J.; Xie, Z. Sierpinski gasket-like Pt-Ag octahedral alloy nanocrystals with enhanced electrocatalytic activity and stability. *Nano Energy* **2019**, *61*, 397–403. [CrossRef]
59. Becknell, N.; Kang, Y.; Chen, C.; Resasco, J.; Kornienko, N.; Guo, J.; Markovic, N.M.; Somorjai, G.A.; Stamenkovic, V.R.; Yang, P. Atomic structure of Pt3Ni nanoframe electrocatalysts by in situ X-ray absorption spectroscopy. *J. Am. Chem. Soc.* **2015**, *137*, 15817–15824. [CrossRef]
60. Becknell, N.; Son, Y.; Kim, D.; Li, D.; Yu, Y.; Niu, Z.; Lei, T.; Sneed, B.T.; More, K.L.; Markovic, N.M.; et al. Control of architecture in rhombic dodecahedral Pt-Ni nanoframe electrocatalysts. *J. Am. Chem. Soc.* **2017**, *139*, 11678–11681. [CrossRef]
61. Chen, C.; Kang, Y.; Huo, Z.; Zhu, Z.; Huang, W.; Xin, H.L.; Snyder, J.D.; Li, D.; Herron, J.A.; Mavrikakis, M.; et al. Highly crystalline multimetallic nanoframes with three-dimensional electrocatalytic surfaces. *Science* **2014**, *343*, 1339–1343. [CrossRef]
62. Chen, S.; Li, M.; Gao, M.; Jin, J.; van Spronsen, M.A.; Salmeron, M.B.; Yang, P. High-performance Pt-Co nanoframes for fuel-cell electrocatalysis. *Nano Lett.* **2020**, *20*, 1974–1979. [CrossRef] [PubMed]
63. Ding, J.; Bu, L.; Guo, S.; Zhao, Z.; Zhu, E.; Huang, Y.; Huang, X. Morphology and phase controlled construction of Pt-Ni nanostructures for efficient electrocatalysis. *Nano Lett.* **2016**, *16*, 2762–2767. [CrossRef] [PubMed]
64. Zhang, N.; Shao, Q.; Xiao, X.; Huang, X. Advanced catalysts derived from composition-segregated platinum-nickel nanostructures: New opportunities and challenges. *Adv. Funct. Mater.* **2019**, *29*, 1808161. [CrossRef]
65. Oezaslan, M.; Hasche, F.; Strasser, P. $PtCu_3$, PtCu and Pt_3Cu alloy nanoparticle electrocatalysts for oxygen reduction reaction in alkaline and acidic media. *J. Electrochem. Soc.* **2012**, *159*, B444–B454. [CrossRef]
66. Oezaslan, M.; Hasche, F.; Strasser, P. Oxygen electroreduction on $PtCo_3$, PtCo and Pt_3Co alloy nanoparticles for alkaline and acidic PEM fuel cells. *J. Electrochem. Soc.* **2012**, *159*, B394–B405. [CrossRef]
67. Oezaslan, M.; Strasser, P. Activity of dealloyed $PtCo_3$ and $PtCu_3$ nanoparticle electrocatalyst for oxygen reduction reaction in polymer electrolyte membrane fuel cell. *J. Power Sources* **2011**, *196*, 5240–5249. [CrossRef]
68. Andersson, K.J.; Calle-Vallejo, F.; Rossmeisl, J.; Chorkendorff, I. Adsorption-driven surface segregation of the less reactive alloy component. *J. Am. Chem. Soc.* **2009**, *131*, 2404–2407. [CrossRef]
69. Jakob, P.; Schlapka, A. CO adsorption on epitaxially grown Pt layers on Ru(0001). *Surf. Sci.* **2007**, *601*, 3556–3568. [CrossRef]
70. Schlapka, A.; Lischka, M.; Groß, A.; Käsberger, U.; Jakob, P. Surface strain versus substrate interaction in heteroepitaxial metal layers: Pt on Ru(0001). *Phys. Rev. Lett.* **2003**, *91*, 016101. [CrossRef]
71. Chen, H.-S.; Benedetti, T.M.; Lian, J.; Cheong, S.; O'mara, P.B.; Sulaiman, K.O.; Kelly, C.H.W.; Scott, R.W.J.; Gooding, J.J.; Tilley, R.D. Role of the secondary metal in ordered and disordered Pt-M intermetallic nanoparticles: An example of Pt3Sn nanocubes for the electrocatalytic methanol oxidation. *ACS Catal.* **2021**, *11*, 2235–2243. [CrossRef]
72. Chen, L.; Zhu, J.; Xuan, C.; Xiao, W.; Xia, K.; Xia, W.; Lai, C.; Xin, H.L.; Wang, D. Effects of crystal phase and composition on structurally ordered Pt-Co-Ni/C ternary intermetallic electrocatalysts for the formic acid oxidation reaction. *J. Mater. Chem. A* **2018**, *6*, 5848–5855. [CrossRef]
73. Chen, M.-X.; Luo, X.; Song, T.-W.; Jiang, B.; Liang, H.-W. Ordering degree-dependent activity of Pt3M (M = Fe, Mn) intermetallic nanoparticles for electrocatalytic methanol oxidation. *J. Phys. Chem. Lett.* **2022**, *13*, 3549–3555. [CrossRef] [PubMed]
74. Chen, W.; Luo, S.; Sun, M.; Tang, M.; Fan, X.; Cheng, Y.; Wu, X.; Liao, Y.; Huang, B.; Quan, Z. Hexagonal PtBi intermetallic inlaid with sub-monolayer Pb oxyhydroxide boosts methanol oxidation. *Small* **2022**, *18*, e2107803. [CrossRef] [PubMed]
75. Di, Q.; Zhao, X.; Zhu, W.; Luan, Y.; Hou, Z.; Fan, X.; Zhou, Y.; Wang, S.; Quan, Z.; Zhang, J. Controllable synthesis of platinum-tin intermetallic nanoparticles with high electrocatalytic performance for ethanol oxidation. *Inorg. Chem. Front.* **2022**, *9*, 1143–1151. [CrossRef]
76. Feng, Q.; Zhao, S.; He, D.; Tian, S.; Gu, L.; Wen, X.; Chen, C.; Peng, Q.; Wang, D.; Li, Y. Strain engineering to enhance the electrooxidation performance of atomic-layer Pt on intermetallic Pt_3Ga. *J. Am. Chem. Soc.* **2018**, *140*, 2773–2776. [CrossRef] [PubMed]
77. Fu, X.; Li, H.; Xu, A.; Xia, F.; Zhang, L.; Zhang, J.; Ma, D.; Wu, J.; Yue, Q.; Yang, X.; et al. Phase engineering of intermetallic PtBi2 nanoplates for formic acid electrochemical oxidation. *Nano Lett.* **2023**, *23*, 5467–5474. [CrossRef]
78. Huang, B.; Ge, Y.; Zhang, A.; Zhu, S.; Chen, B.; Li, G.; Yun, Q.; Huang, Z.; Shi, Z.; Zhou, X.; et al. Seeded synthesis of hollow PdSn intermetallic nanomaterials for highly efficient electrocatalytic glycerol oxidation. *Adv. Mater.* **2023**, *35*, e2302233. [CrossRef]

79. Nie, Y.; Qi, X.; Wu, R.; Yang, R.; Wang, H.; Deng, M.; Zhang, S.; Lu, S.; Gu, Z.; Liu, X. Structurally ordered PtFe intermetallic nanocatalysts toward efficient electrocatalysis of methanol oxidation. *Appl. Surf. Sci.* **2021**, *569*, 151004. [CrossRef]
80. Qin, Y.; Luo, M.; Sun, Y.; Li, C.; Huang, B.; Yang, Y.; Li, Y.; Wang, L.; Guo, S. Intermetallic hcp-PtBi/fcc-Pt core/shell nanoplates enable efficient bifunctional oxygen reduction and methanol oxidation electrocatalysis. *ACS Catal.* **2018**, *8*, 5581–5590. [CrossRef]
81. Zhang, B.-W.; Lai, W.-H.; Sheng, T.; Qu, X.-M.; Wang, Y.-X.; Ren, L.; Zhang, L.; Du, Y.; Jiang, Y.-X.; Sun, S.-G.; et al. Ordered platinum-bismuth intermetallic clusters with Pt-skin for a highly efficient electrochemical ethanol oxidation reaction. *J. Mater. Chem. A* **2019**, *7*, 5214–5220. [CrossRef]
82. Zhu, J.; Yang, Y.; Chen, L.; Xiao, W.; Liu, H.; Abruña, H.D.; Wang, D. Copper-induced formation of structurally ordered Pt-Fe-Cu ternary intermetallic electrocatalysts with tunable phase structure and improved stability. *Chem. Mater.* **2018**, *30*, 5987–5995. [CrossRef]
83. Chen, W.; Luo, S.; Sun, M.; Wu, X.; Zhou, Y.; Liao, Y.; Tang, M.; Fan, X.; Huang, B.; Quan, Z. High-entropy intermetallic PtRhBiSnSb nanoplates for highly efficient alcohol oxidation electrocatalysis. *Adv. Mater.* **2022**, *34*, e2206276. [CrossRef]
84. Li, J.; Sun, S. Intermetallic nanoparticles: Synthetic control and their enhanced electrocatalysis. *Acc. Chem. Res.* **2019**, *52*, 2015–2025. [CrossRef] [PubMed]
85. Li, J.; Xi, Z.; Pan, Y.-T.; Spendelow, J.S.; Duchesne, P.N.; Su, D.; Li, Q.; Yu, C.; Yin, Z.; Shen, B.; et al. Fe Stabilization by Intermetallic L1(0)-FePt and Pt Catalysis Enhancement in L1(0)-FePt/Pt Nanoparticles for Efficient Oxygen Reduction Reaction in Fuel Cells. *J. Am. Chem. Soc.* **2018**, *140*, 2926–2932. [CrossRef] [PubMed]
86. Bu, L.; Zhang, N.; Guo, S.; Zhang, X.; Li, J.; Yao, J.; Wu, T.; Lu, G.; Ma, J.-Y.; Su, D.; et al. Biaxially strained PtPb/Pt core/shell nanoplate boosts oxygen reduction catalysis. *Science* **2016**, *354*, 1410–1414. [CrossRef]
87. Li, J.; Jilani, S.Z.; Lin, H.; Liu, X.; Wei, K.; Jia, Y.; Zhang, P.; Chi, M.; Tong, Y.J.; Xi, Z.; et al. Ternary CoPtAu nanoparticles as a general catalyst for highly efficient electro-oxidation of liquid fuels. *Angew. Chem. Int. Ed.* **2019**, *58*, 11527–11533. [CrossRef]
88. Escudero-Escribano, M.; Malacrida, P.; Hansen, M.H.; Vej-Hansen, U.G.; Velázquez-Palenzuela, A.; Tripkovic, V.; Schiøtz, J.; Rossmeisl, J.; Stephens, I.E.L.; Chorkendorff, I. Tuning the activity of Pt alloy electrocatalysts by means of the lanthanide contraction. *Science* **2016**, *352*, 73–76. [CrossRef]
89. Zhang, S.; Zeng, Z.; Li, Q.; Huang, B.; Zhang, X.; Du, Y.; Yan, C.-H. Lanthanide electronic perturbation in Pt-Ln (La, Ce, Pr and Nd) alloys for enhanced methanol oxidation reaction activity. *Energy Environ. Sci.* **2021**, *14*, 5911–5918. [CrossRef]
90. Fan, C.; Wen, P.; Li, G.; Li, G.; Gu, J.; Li, Q.; Li, B. Facile synthesis of Pt5La nanoalloys as the enhanced electrocatalysts for oxygen reduction reaction and methanol oxidation reaction. *J. Alloy. Compd.* **2022**, *894*, 161892. [CrossRef]
91. Cui, Z.; Chen, H.; Zhao, M.; Marshall, D.; Yu, Y.; Abruna, H.; DiSalvo, F.J. Synthesis of structurally ordered Pt3Ti and Pt3V nanoparticles as methanol oxidation catalysts. *J. Am. Chem. Soc.* **2014**, *136*, 10206–10209. [CrossRef]
92. Li, Q.; Wu, L.; Wu, G.; Su, D.; Lv, H.; Zhang, S.; Zhu, W.; Casimir, A.; Zhu, H.; Mendoza-Garcia, A.; et al. New approach to fully ordered fct-FePt nanoparticles for much enhanced electrocatalysis in acid. *Nano Lett.* **2015**, *15*, 2468–2473. [CrossRef] [PubMed]
93. Liang, J.; Li, N.; Zhao, Z.; Ma, L.; Wang, X.; Li, S.; Liu, X.; Wang, T.; Du, Y.; Lu, G.; et al. Tungsten-doped L10-PtCo ultrasmall nanoparticles as a high-performance fuel cell cathode. *Angew. Chem. Int. Ed.* **2019**, *58*, 15471–15477. [CrossRef] [PubMed]
94. Wang, X.; Xie, M.; Lyu, F.; Yiu, Y.-M.; Wang, Z.; Chen, J.; Chang, L.-Y.; Xia, Y.; Zhong, Q.; Chu, M.; et al. Bismuth oxyhydroxide-Pt inverse interface for enhanced methanol electrooxidation performance. *Nano Lett.* **2020**, *20*, 7751–7759. [CrossRef]
95. Yuan, X.; Zhang, Y.; Cao, M.; Zhou, T.; Jiang, X.; Chen, J.; Lyu, F.; Xu, Y.; Luo, J.; Zhang, Q.; et al. Bi(OH)(3)/PdBi composite nanochains as highly active and durable electrocatalysts for ethanol oxidation. *Nano Lett.* **2019**, *19*, 4752–4759. [CrossRef]
96. Chen, Z.; Liu, Y.; Liu, C.; Zhang, J.; Chen, Y.; Hu, W.; Deng, Y. Engineering the metal/oxide interface of Pd nanowire@CuOx electrocatalysts for efficient alcohol oxidation reaction. *Small* **2020**, *16*, 1904964. [CrossRef]
97. Tao, L.; Shi, Y.; Huang, Y.-C.; Chen, R.; Zhang, Y.; Huo, J.; Zou, Y.; Yu, G.; Luo, J.; Dong, C.-L.; et al. Interface engineering of Pt and CeO_2 nanorods with unique interaction for methanol oxidation. *Nano Energy* **2018**, *53*, 604–612. [CrossRef]
98. Li, C.; Huang, B.; Luo, M.; Qin, Y.; Sun, Y.; Li, Y.; Yang, Y.; Wu, D.; Li, M.; Guo, S. An efficient ultrathin PtFeNi nanowire/ionic liquid conjugate electrocatalyst. *Appl. Catal. B Environ.* **2019**, *256*, 117828. [CrossRef]
99. Huang, L.; Zhang, X.; Wang, Q.; Han, Y.; Fang, Y.; Dong, S. Shape-control of Pt-Ru nanocrystals: Tuning surface structure for enhanced electrocatalytic methanol oxidation. *J. Am. Chem. Soc.* **2018**, *140*, 1142–1147. [CrossRef]
100. Kang, Y.; Li, M.; Cai, Y.; Cargnello, M.; Diaz, R.E.; Gordon, T.R.; Wieder, N.L.; Adzic, R.R.; Gorte, R.J.; Stach, E.A.; et al. Heterogeneous catalysts need not be so "heterogeneous": Monodisperse Pt nanocrystals by combining shape-controlled synthesis and purification by colloidal recrystallization. *J. Am. Chem. Soc.* **2013**, *135*, 2741–2747. [CrossRef]
101. Li, C.; Chen, X.; Zhang, L.; Yan, S.; Sharma, A.; Zhao, B.; Kumbhar, A.; Zhou, G.; Fang, J. Synthesis of core@shell Cu-Ni@Pt-Cu nano-octahedra and their improved MOR activity. *Angew. Chem. Int. Ed.* **2021**, *60*, 7675–7680. [CrossRef]
102. Huang, L.; Zheng, C.Y.; Shen, B.; Mirkin, C.A. High-index-facet metal-alloy nanoparticles as fuel cell electrocatalysts. *Adv. Mater.* **2020**, *32*, 2002849. [CrossRef] [PubMed]
103. Shen, B.; Huang, L.; Shen, J.; He, K.; Zheng, C.Y.; Dravid, V.P.; Wolverton, C.; Mirkin, C.A. Crystal structure engineering in multimetallic high-index facet nanocatalysts. *Proc. Natl. Acad. Sci. USA* **2021**, *118*, e2105722118. [CrossRef]
104. Huang, L.; Lin, H.; Zheng, C.Y.; Kluender, E.J.; Golnabi, R.; Shen, B.; Mirkin, C.A. Multimetallic high-index faceted heterostructured nanoparticles. *J. Am. Chem. Soc.* **2020**, *142*, 4570–4575. [CrossRef] [PubMed]

105. Song, Y.; Bi, C.; Wu, C.; He, H.; Huang, L.; Wang, D.; Xia, H. Promoting charge transfer in hyperbranched, trisoctahedral-shaped core-shell Au@PdPt nanoparticles by facet-dependent construction of transition layers as high performance electrocatalysts. *J. Mater. Chem. A* **2017**, *5*, 18878–18887. [CrossRef]
106. Huang, L.; Zhang, X.; Han, Y.; Wang, Q.; Fang, Y.; Dong, S. High-index facets bounded platinum-lead concave nanocubes with enhanced electrocatalytic properties. *Chem. Mater.* **2017**, *29*, 4557–4562. [CrossRef]
107. Li, Y.; Wang, Y.; Li, S.; Li, M.; Liu, Y.; Fang, X.; Dai, X.; Zhang, X. Pt3Mn alloy nanostructure with high-index facets by Sn doping modified for highly catalytic active electro-oxidation reactions. *J. Catal.* **2021**, *395*, 282–292. [CrossRef]
108. Luo, M.; Sun, Y.; Zhang, X.; Qin, Y.; Li, M.; Li, Y.; Li, C.; Yang, Y.; Wang, L.; Gao, P.; et al. Stable high-index faceted Pt skin on zigzag-like PtFe nanowires enhances oxygen reduction catalysis. *Adv. Mater.* **2018**, *30*, 1705515. [CrossRef]
109. Quan, Z.; Wang, Y.; Fang, J. High-index faceted noble metal nanocrystals. *Acc. Chem. Res.* **2013**, *46*, 191–202. [CrossRef]
110. Feng, G.; Ning, F.; Pan, Y.; Chen, T.; Song, J.; Wang, Y.; Zou, R.; Su, D.; Xia, D. Engineering structurally ordered high-entropy intermetallic nanoparticles with high-activity facets for oxygen reduction in practical fuel cells. *J. Am. Chem. Soc.* **2023**, *145*, 11140–11150. [CrossRef]
111. Feng, G.; Ning, F.; Song, J.; Shang, H.; Zhang, K.; Ding, Z.; Gao, P.; Chu, W.; Xia, D. Sub-2 nm ultrasmall high-entropy alloy nanoparticles for extremely superior electrocatalytic hydrogen evolution. *J. Am. Chem. Soc.* **2021**, *143*, 17117–17127. [CrossRef]
112. Wu, D.; Kusada, K.; Yamamoto, T.; Toriyama, T.; Matsumura, S.; Gueye, I.; Seo, O.; Kim, J.; Hiroi, S.; Sakata, O.; et al. On the electronic structure and hydrogen evolution reaction activity of platinum group metal-based high-entropy-alloy nanoparticles. *Chem. Sci.* **2021**, *12*, 7196. [CrossRef] [PubMed]
113. Wu, D.; Kusada, K.; Yamamoto, T.; Toriyama, T.; Matsumura, S.; Kawaguchi, S.; Kubota, Y.; Kitagawa, H. Platinum-group-metal high-entropy-alloy nanoparticles. *J. Am. Chem. Soc.* **2020**, *142*, 13833–13838. [CrossRef] [PubMed]
114. Bueno, S.L.A.; Leonardi, A.; Kar, N.; Chatterjee, K.; Zhan, X.; Chen, C.; Wang, Z.; Engel, M.; Fung, V.; Skrabalak, S.E. Quinary, senary, and septenary high entropy alloy nanoparticle catalysts from core@shell nanoparticles and the significance of intraparticle heterogeneity. *ACS Nano* **2022**, *16*, 18873–18885. [CrossRef] [PubMed]
115. Amiri, A.; Shahbazian-Yassar, R. Recent progress of high-entropy materials for energy storage and conversion. *J. Mater. Chem. A* **2021**, *9*, 782–823. [CrossRef]
116. Xin, Y.; Li, S.; Qian, Y.; Zhu, W.; Yuan, H.; Jiang, P.; Guo, R.; Wang, L. High-entropy alloys as a platform for catalysis: Progress, challenges, and opportunities. *ACS Catal.* **2020**, *10*, 11280–11306. [CrossRef]
117. Zhao, P.; Cao, Q.; Yi, W.; Hao, X.; Li, J.; Zhang, B.; Huang, L.; Huang, Y.; Jiang, Y.; Xu, B.; et al. Facile and general method to synthesize Pt-based high-entropy-alloy nanoparticles. *ACS Nano* **2022**, *16*, 14017–14028. [CrossRef]
118. Wang, D.; Chen, Z.; Huang, Y.-C.; Li, W.; Wang, J.; Lu, Z.; Gu, K.; Wang, T.; Wu, Y.; Chen, C.; et al. Tailoring lattice strain in ultra-fine high-entropy alloys for active and stable methanol oxidation. *Sci. China Mater.* **2021**, *64*, 2454–2466. [CrossRef]
119. Zhang, N.; Bu, L.; Guo, S.; Guo, J.; Huang, X. Screw thread-like platinum-copper nanowires bounded with high index facets for efficient electrocatalysis. *Nano Lett.* **2016**, *16*, 5037–5043. [CrossRef]
120. Chen, X.; Wang, W.; Chen, X.-J.; Liao, X.; Lyu, Z.; Liu, K.; Xie, S. Structure-intensified PtCoRh spiral nanowires as highly active and durable electrocatalysts for methanol oxidation. *Nanoscale* **2021**, *13*, 2632–2638. [CrossRef]
121. Xu, Y.; Cui, X.; Wei, S.; Zhang, Q.; Gu, L.; Meng, F.; Fan, J.; Zheng, W. Highly active zigzag-like Pt-Zn alloy nanowires with high-index facets for alcohol electrooxidation. *Nano Res.* **2019**, *12*, 1173–1179. [CrossRef]
122. Sun, Y.; Liang, Y.; Luo, M.; Lv, F.; Qin, Y.; Wang, L.; Xu, C.; Fu, E.; Guo, S. Defects and interfaces on PtPb nanoplates boost fuel cell electrocatalysis. *Small* **2017**, *14*, 1702259. [CrossRef] [PubMed]
123. Huang, J.; Liu, Y.; Xu, M.; Wan, C.; Liu, H.; Li, M.; Huang, Z.; Duan, X.; Pan, X.; Huang, Y. PtCuNi tetrahedra catalysts with tailored surfaces for efficient alcohol oxidation. *Nano Lett.* **2019**, *19*, 5431–5436. [CrossRef] [PubMed]
124. Maya-Cornejo, J.; Garcia-Bernabé, A.; Compañ, V. Bimetallic Pt-M electrocatalysts supported on single-wall carbon nanotubes for hydrogen and methanol electrooxidation in fuel cells applications. *Int. J. Hydrogen Energy* **2018**, *43*, 872–884. [CrossRef]